This is the peer-reviewed, final accepted version for American Mineralogist, published by the Mineralogical Society of America.
The published version is subject to change. Cite as Authors (Year) Title. American Mineralogist, in press.
DOI: https://doi.org/10.2138/am-2022-8201. http://www.minsocam.org/

REVISION 1

- Word count: 11 330 total (8 509 abstract and main text + 2 821 references)

Paragenesis and precipitation stages of Nb-Ta-oxide minerals in phosphorus-rich rare-element pegmatites (Buranga dike, Rwanda)

Fernando Prado Araujo[1*], Niels Hulsbosch[1], and Philippe Muchez[1]

[1]KU Leuven, Department of Earth and Environmental Sciences & Institute for Sustainable Metals and Minerals. Celestijnenlaan 200E - Box 2410, 3001 Leuven, Belgium (*corresponding author: fernando.pradoaraujo@kuleuven.be)

ABSTRACT

Nb-Ta-oxide minerals (NTO) are commonly associated with rare-element pegmatites where they are interpreted to precipitate at magmatic up to magmatic-hydrothermal conditions. Although high-temperature experiments show that phosphorus and other fluxing elements (e.g., Li, B, F) can affect the saturation of NTO in pegmatitic systems, it is still uncertain how NTO saturation occurs in natural, flux-rich pegmatitic melts and whether crystallization occurs at multiple stages during magmatic or subsolidus conditions. The LCT family P-rich Buranga granitic pegmatite (western Rwanda) is used as a type locality to address this question. NTO mineralization in the Buranga dike occurs in two mineralogical units: in mineralogically complex phosphatic nodules, and in albitized parts. In the phosphatic nodules, Fe-Nb-Ta-rich rutile and columbite-group minerals (CGM) are observed, while in the albitized parts, only CGM is found. Fe-Nb-Ta-rich rutile precipitates at the magmatic stage along with early primary phosphates (i.e., F-rich montebrasite, wyllieite, and fluorapatite). Conversely, CGM mineralization occurs at the magmatic-hydrothermal stage in association with replacement phosphates like bertossaite, after primary minerals (i.e., rutile, wyllieite, rosemaryite, and trolleite) are destabilized due to crystal-melt-fluid interactions. NTO textures and chemical zoning show uneven evolution from core to rim and are related to localized alteration phenomena of the surrounding minerals. This indicates that local processes and element transfers are more important than dike-scale fractionation processes for NTO mineralization in P-rich granitic pegmatites. The restricted availability of Fe and Mn in the system, which is related to the competition between phosphate and oxide minerals, is identified as the main control on the CGM mineralization in the Buranga dike. CGM precipitation is only

possible during the magmatic-hydrothermal stage when Fe and Mn are leached from the primary phosphates and remobilized to the Nb-Ta-bearing residual melt by the exsolved fluid.

Keywords: Nb-Ta mineralization, granitic pegmatite, pegmatitic phosphates, mineral paragenesis, Raman mapping, Buranga pegmatite

1. INTRODUCTION

Rare-element granitic pegmatites are commonly enriched in incompatible elements, e.g., Li, Rb, Cs, Be, Ta, Nb, P, and B (Černý et al. 1985; London 1987; Linnen and Cuney 2005; Simmons and Webber 2008). Most of the large-scale melt differentiation and element enrichment can be explained by fractional crystallization in a residual melt segregated from granitic mushes (Raimbault et al. 1995; Hulsbosch et al. 2014; Stepanov et al. 2014). However, the extreme elemental enrichment and fractionation of particular geochemical ratios (i.e., Nb/Ta) observed in some pegmatites cannot be attributed to a pure equilibrium fractional crystallization model (Van Lichtervelde et al. 2018; Ballouard et al. 2020b; Kaeter et al. 2021). Therefore, additional mechanisms are required to explain this fractionation, especially on the scale of an individual pegmatite dike.

Due to their identical charge and similar ionic radius (i.e., usually labeled "geochemical twins"), Nb and Ta are not expected to fractionate extensively in most geological environments, requiring specific processes to fractionate (Green 1995). Nonetheless, niobium-tantalum-oxide minerals (NTO) commonly record considerable degrees of Nb/Ta fractionation in pegmatitic systems (e.g., Černý and Ercit 1985; Beurlen et al. 2008; Wise et al. 2012; Fuchsloch et al. 2019). This can be related to the lower solubility of $MnNb_2O_6$ to $MnTa_2O_6$ (Linnen 1998), suggesting that the melt Nb/Ta ratio decreases during magmatic differentiation until saturation of tantalite is reached. Contrarily, if saturation is not reached, the metals can be incorporated into other minerals (especially Fe-Ti oxides, micas, and phosphates).

Overall, the reported content of Nb and Ta in pegmatitic melts (Webster et al. 1997; Borisova et al. 2012) is mostly below the necessary saturation values for NTO (Linnen and Keppler 1997; Linnen 1998; London 2018; Van Lichtervelde et al. 2018; McNeil et al. 2020). This resulted in multiple hypotheses for the

precipitation of NTO in pegmatites. The mineralization can be purely magmatic, originating from fractional crystallization (Černý et al. 1986; Llorens et al. 2017), due to extreme undercooling and disequilibrium crystallization (London 2018; Van Lichtervelde et al. 2018) or chemical quenching (Linnen et al. 2012). Alternatively, it can be triggered by interactions with an aqueous fluid phase (Ballouard et al. 2020b; Kaeter et al. 2021), possibly due to the remobilization of the mobile major elements present in NTO (i.e., Fe and Mn) into the melt (McNeil et al. 2020).

Nb and Ta mineralization is commonly associated with residual melts enriched in fluxing elements, e.g., Li, B, P, and F (Černý et al. 1985; Linnen 1998; London 2018; Araujo et al. 2020), which can considerably lower the melt solidus and facilitate mineral saturation (London 1987; Bartels et al. 2010; Fiege et al. 2018). Additionally, experiments show that phosphorus is incompatible during crystallization, and its content should increase until a phosphate phase becomes stable (London et al. 1993). Hence, the crystallization of phosphate minerals should directly impact the saturation of NTO in the melt, both by controlling the availability of fluxes (P and Li) and other relevant elements in the melt, e.g., Fe and Mn.

The crystallization of phosphorus-rich pegmatitic melts can result in a complex paragenetic sequence with numerous phosphate minerals (Moore 1973; Fransolet 1980; London and Burt 1982; Roda et al. 2004; Galliski et al. 2012; Baijot et al. 2014; Araujo et al. 2021). Although individual phosphate minerals or specific assemblages can have narrow pressure-temperature-composition (P-T-X) stability fields (Bass and Sclar 1979; Schmid-Beurmann et al. 2000; Hatert et al. 2006, 2011a). Therefore, phosphates are sensitive to physicochemical changes during crystallization and record the magmatic stage, the magmatic-hydrothermal transition, and the subsolidus alteration processes in pegmatites (Moore 1973). The mineral parageneses often record a sequence of chemical reactions that occurred during cooling, such as leaching of elements (e.g., Li, F), hydration, oxidation, and other cation exchanges (e.g., Na, Ca, Fe, Mn, Ba) (Fisher 1958; Moore 1973; Roda-Robles et al. 2010; Baijot et al. 2014). Consequently, since phosphate minerals cover the full crystallization spectrum, and can be paragenetically linked to NTO, they are valuable tools to investigate the processes leading to NTO mineralization.

The Buranga pegmatite, located in the Gatumba Pegmatite District of Western Rwanda, is an outstanding natural case study to assess the relation between enrichment in fluxing agents (P, Li, B, etc.) and rare-metal mineralization. The dike is a highly evolved phosphorus-rich LCT pegmatite and is mineralized in Nb, Ta, and Sn, with currently artisanal miners exploiting outcropping zones for rare metals (Dewaele et al. 2011; Muchez et al. 2014).

This contribution investigates the textural, major elemental, and Raman spectroscopic variations of Nb-Ta-oxide minerals and their host phases crystallizing in the phosphorus-rich Buranga pegmatite aiming 1) to understand the setting in which the saturation of ore minerals took place, whether directly in a magmatic environment or during the magmatic-hydrothermal transition under the influence of interactions between melt, crystals, and fluid, and 2) to assess if the host phosphate minerals can be used as proxies to constrain the crystallization of Nb-Ta-oxide minerals, providing a natural counterpart for Nb-Ta solubility experiments in pegmatitic melts.

2. GEOLOGICAL SETTING

2.1. Regional context

The study area is part of the Karagwe-Ankole Belt (KAB) in central Africa (Tack et al. 2010; Fernandez-Alonso et al. 2012; Van Daele et al. 2020) where many pegmatite fields are recognized. These pegmatites are linked to the Neoproterozoic, ca. 1000–900 Ma, "Kibara tin granites" (Pohl et al. 2013; Melcher et al. 2015; Hulsbosch 2019) and they include the Gitarama-Gatumba field (Fig. 1) as one of the best representatives of the magmatic evolution and the related rare-metal mineralization (Dewaele et al. 2011; Hulsbosch et al. 2014, 2016).

The Gitarama-Gatumba field encompasses pegmatite bodies spatially zoned around S-type composite batholiths (Varlamoff 1972; Muchez et al. 2014), ranging from (1) biotite pegmatites to (2) two-mica pegmatites, (3) muscovite pegmatites, and finally (4) Nb-Ta-Sn-mineralized pegmatites (Hulsbosch et al. 2013). Chemical analyses of rock-forming minerals show that this zonation follows a magmatic fractionation

trend, where the mineralized pegmatites, which are enriched in Li, Be, B and P, represent the last melt fraction extracted from the granitic mush (Hulsbosch et al. 2014).

2.2. Buranga pegmatite

The samples for this study are from the Buranga dike, located in the Gitarama-Gatumba pegmatite field of Western Rwanda (Dewaele et al. 2011). The Buranga pegmatite is a phosphorus-rich dike with affinity to the LCT (Li-Cs-Ta) family. It hosts more than 50 phosphate minerals (Daltry and von Knorring 1998) and is the type locality for three of them: bertossaite [$(Li,Na)_2(Ca,Fe^{2+},Mn^{2+})Al_4(PO_4)_4(OH,F)_4$], burangaite [$NaFe^{2+}Al_5(PO_4)_4(OH)_6.2H_2O$], and gatumbaite [$CaAl_2(PO_4)_2(OH)_2.H_2O$]. For a mineralogical overview of all the minerals described in the Buranga dike, the reader is referred to Daltry and von Knorring (1998).

The Buranga dike measures around 250 m in its long axis, 200 m in the short axis, and 20 m in depth (Fig. 2). The dike is strongly asymmetric in respect to its fairly marked internal zones (Fransolet 1975). The pegmatite is hosted by tourmalinized country rocks, namely metasedimentary (mica schists and quartzites) to the east and (meta)-mafic rocks (gabbro to amphibolite) to the west (Polinard 1950). The dike is enclosed by a fine- to medium-grained border zone presenting K-feldspar, quartz, Li-rich muscovite, and tourmaline. Following, a wall zone dominated by large blocky and coarse-grained crystals of the same mineralogy is present. The wall zone transitions into an intermediate zone with massive crystals of lithium minerals (e.g., amblygonite-montebrasite and spodumene), multi-colored beryl, and apatite (Varlamoff 1961, 1972). This intermediate zone has undergone moderate secondary alteration, including albitization with saccharoidal or platy (cleavelandite) albite textures, and greisenization marked by a muscovite-quartz assemblage (Varlamoff 1963, 1972; Fransolet 1975). Finally, a distinctive, roughly 15 m wide, quartz-rich core zone occurs closer to the eastern border (Fig. 2).

Phosphate minerals occur as polymineralic nodules in the core zone and the transition region between the intermediate and core zones (Fransolet 1975), something that is not commonly seen in other pegmatites of the region (Varlamoff 1972; Dewaele et al. 2011). Two groups of phosphate nodules are described (Polinard 1950; Daltry and von Knorring 1998): (1) massive blocks of several cubic decimeters dominated by

white montebrasite, with other Al-rich phosphates; (2) massive associations of multiple dark-colored Fe-Mn-rich phosphates dominated by lithiophilite-triphyllite.

Ore mineral concentrates from Buranga are dominated by columbite-group minerals (CGM), with traces of microlite, tapiolite, cassiterite, rutile, wodginite, and ixiolite (Melcher et al. 2015). Most of these are found within the albitized intermediate zone (Varlamoff 1963). The precipitation of CGM and some cassiterite has been suggested to pre-date the albitization event, with CGM crystals providing U-Pb ages of 936 ± 14 Ma (upper Discordia intercept), while the main cassiterite mineralization is associated with greisenization pockets (Dewaele et al. 2011). The CGM ages are slightly younger than ages obtained in the surrounding granites, ~1020-950 Ma by zircon U-Pb dating (Tack et al. 2010; De Clercq et al. 2021; Nambaje et al. 2021), but are within the age range of 975 ± 29 Ma to 940 ± 28 Ma obtained in the pegmatite dikes by muscovite Rb-Sr dating (Monteyne-Poulaert et al. 1963). Recent studies of the mineralization in the Gitarama-Gatumba field point to a more complex mineralization history, with at least three generations of cassiterite formed from a water-saturated melt system, and triggered initially by local disequilibrium around the fast-growing pegmatitic minerals or lately by metasomatic fluid-rock interactions (Hulsbosch and Muchez 2020). Similarly, new cassiterite U-Pb dating at ca. 1150–1140 Ma inside the pegmatites, and ca. 1090–960 Ma in the main Sn mineralization in quartz veins and intra-pegmatitic greisen (Nambaje et al. 2021), points to older crystallization ages in the region.

3. METHODOLOGY

3.1. Materials and sample location

The NTO ore minerals of the Buranga dike were found in two settings: either associated with phosphate minerals in phosphatic nodules (samples BU02, BU04, BU19) or with silicate minerals in albitization zones (samples BU12, BU24, BU25). The samples are part of historical collections and were retrieved from the Royal Museum for Central Africa mineral and rock collection and from the University of Liège collection. Although the precise location coordinates of the samples are unknown, documents describe that phosphatic nodules come from close to the quartz core, and the albitized specimens from the alteration section in the

intermediate zone. Samples were prepared into polished thin sections (30-50 μm) for transmitted- and reflected-light optical analyses, conducted on an Olympus BX40 petrographic polarization microscope at the Department of Earth and Environmental Sciences, KU Leuven, Belgium. The same thin sections were subsequently analyzed by Raman spectroscopy and field emission gun electron probe micro-analyzer.

3.2. Mineral chemistry

Major element composition of NTO was measured in situ by energy-dispersive spectroscopy (EDS) and wavelength-dispersive spectroscopy (WDS) with a JEOL JXA-8530F field emission gun electron probe micro-analyzer (FEG-EPMA) at the Department of Materials Engineering, KU Leuven, Belgium. More details on the equipment can be found in Van Daele et al. (2020). Samples were coated with a ~20 nm layer of carbon and imaged by backscattered electrons (BSE) before point analyses. EDS data were acquired with a silicon drift type detector, cooled by Peltier effect, under an acceleration voltage of 15 kV and beam current of 10 nA. WDS analyses were acquired with an accelerating voltage of 20 kV, 40 nA beam current, and 1 μm spot size. The JEOL's internal PRZ correction (Armstrong 1991) was applied to quantify the composition of unknown samples using as standards: (TAP crystal) Al-Kα on almandine, Ta-Mα on metallic tantalum; (PETJ crystal) Ti-Kα on rutile, Mn-Kα on rhodonite; (TAPH crystal) Mg-Kα on periclase; (LiFH crystal) Fe-Kα on magnetite; (PETH crystal) Sn-Lα on cassiterite, Nb-Lα on metallic niobium, and Ca-Kα on almandine. The peak signal counting time for rutile analysis was 20 s for Al, Ti, Mn, and Mg; 30 s for Ta, Sn, and Nb; 40 s for Fe. For CGM counting times on peaks was 20 s for Nb, Ta, Al, Fe, Mn, and Mg; 30 s for Ti and Sn; 10 s for Ca. In all cases, the high and low background signal was measured for half of the peak time. Mineral formulae were recalculated on the basis of 24 oxygens for 12 cations. The Python scripts used for the processing of element mass% into apfu and graph plotting are available at a dedicated GitLab repository (https://gitlab.com/thembubbles/nto-paragenesis-buranga-pegmatite/).

3.3. Raman microscopy

Raman spectra were obtained using a Horiba Jobin-Yvon LabRAM HR Evolution spectrometer at the Department of Chemistry of KU Leuven. Samples were excited with a Nd:YAG 532 nm wavelength laser

This is the peer-reviewed, final accepted version for American Mineralogist, published by the Mineralogical Society of America.
The published version is subject to change. Cite as Authors (Year) Title. American Mineralogist, in press.
DOI: https://doi.org/10.2138/am-2022-8201. http://www.minsocam.org/

(Oxxius, 100 mW power) combined with laser attenuation filters (modulating the power to 100 %, 50 %, or 10 % of the source) to avoid damaging the samples. In cases where photoluminescence occurred, samples were analyzed using a He-Ne 633 nm wavelength laser (LASOS, 17 mW power).

Point analyses were measured using a 100x (Olympus, NA 0.9) or a 50x long-working distance (Olympus, NA 0.5) microscope objective, 150 grooves/mm grating, and a confocal pinhole aperture of 30 to 50 μm. The integration time of single analyses was 10 s to 40 s depending on the laser power filter used in each analysis (i.e., lower power required longer acquisitions), with two accumulations in the same spot.

Raman maps were acquired using a 50x long-working distance objective in a line-scan mapping array (Horiba SWIFT®). Considering that each Raman map covered different minerals and areas, the required settings also varied. Analytical conditions varied from 0.2 s to 0.5 s single accumulations, arranged in regularly-spaced arrays (2 x 2 or 5 x 5 μm), electron-multiplying gain between 300-800, 30-100 μm confocal pinhole, 150 grooves/mm grating with a range from 100 to 4000 cm^{-1}. The specific analytical settings for each map can be found in their respective legends.

A spike filter was automatically applied during the analysis. Point analyses were subtracted by a 6-degree polynomial baseline with 50 attaching points. The mapping datasets had a 6-degree polynomial baseline subtraction with 150 attaching points, and a range reduction retaining only data between 400 and 3650 cm^{-1}. All Raman images in this manuscript were smoothed to improve the visualization of mineral contacts and to remove rastering effects. Visible and hidden peaks were fitted with Gaussian-Lorentz curves using the PeakFit, v.4.12 (SYSTAT Inc.). Fitting followed the automated procedure using the residuals method. The reader is referred to Araujo et al. (2021) for details on the Raman instrumentation, methodology, calibration, and processing procedures used in this study.

Raman spectroscopy was used in addition to petrography to identify the mineral phases, especially the late phosphates. Raman analyses were carried out before the EPMA analyses to avoid any interference of the carbon coating and damage by the electron beam.

4. RESULTS

4.1. Petrography

NTO mineralization in the Buranga dike occurs in two settings: 1) in mineralogically complex phosphatic nodules (Fig. 3a and b), containing several phosphate minerals, and 2) in albitized facies (Fig. 3c), composed mostly of albite. The complete petrographic description of the minerals observed can be found in the supplementary files S1.

4.1.1. Phosphatic nodules. This facies is composed dominantly of phosphate minerals, with quartz occurring as the main silicate phase along with rare muscovite. Two main associations occur in the Buranga nodules, either dominated by Al-rich phosphates or by Fe-Mn-rich phosphates. Al-rich nodules contain abundant montebrasite, trolleite, bertossaite, scorzalite, and brazilianite, with several minor and accessory phases associated. Fe-Mn-rich nodules are dominated by lithiophilite-triphylite, heterosite-purpurite, rockbridgeite-frondelite, alluaudite, hureaulite, phosphosiderite, and many other minor minerals. Mixtures of the two associations are rare, but in this case, mostly comprise coarse-grained montebrasite in contact with Fe-Mn-rich nodules.

All samples show extensive alteration where primary minerals are replaced by a wide range of secondary phases. Some samples (Fig. 3a) partially retain the primary phosphates and show secondary minerals at their rims, in fractures, and alterations caps, while others (Fig. 3b) are strongly altered presenting mostly secondary phosphates replacing sparse primary phases. These two groups, partially altered and strongly altered nodules, are unevenly distributed, with the Fe-Mn-rich association being much more diversified in their secondary mineralogy than the Al-rich nodules.

Nb-Ta-oxide minerals have been observed only in the Al-rich nodules, implying some genetic relation (see discussion section 5.2 for interpretation). Consequently, this contribution focuses on this association. Al-rich phosphatic nodules show isotropic fabrics and can vary in color from whitish and blueish to pale greenish, brownish, cream-colored, or dark shades of blue. Crystal sizes and shapes are extremely variable, with usually few coarse-grained primary minerals being fractured and replaced by multiple smaller secondary

225 phases. The distinction between primary and secondary minerals is based on crystal textural features, such as
226 shape, size, and especially its relation to adjacent minerals.

227 *4.1.1.1. Phosphate minerals.* A series of phosphate minerals is present in the Al-rich nodules from the
228 Buranga dike (Fig. 4). These were subdivided according to their textural relations into four texture groups.

229 1) The early primary phases are commonly coarse- to medium-grained (>2 cm to 5 mm), frequently
230 altered, and often occur included in later minerals. Early primary minerals are usually euhedral to subhedral,
231 but they can also be anhedral due to alteration (Fig. 5a and b). Wyllieite, F-rich montebrasite, fluorapatite,
232 and rosemaryite are defined as early primary phases. Primary fluid inclusions are rare or absent in these early
233 minerals.

234 2) Late primary minerals show variable crystal sizes, ranging from coarse- to fine-grained (>2 cm to 1
235 mm), and are commonly partially altered. They are mainly subhedral (Fig. 6a and b), but also appear
236 anhedral due to fracturing and alteration by later phases (Figs. 5c and 6c). An important aspect introduced
237 from this group onwards is the widespread occurrence of primary fluid inclusions either following growth
238 zones (Fig. 5d) or more commonly as isolated, irregular three-dimensional clusters. Trolleite is representative
239 of the late primary phases. Muscovite and quartz are also included in this group.

240 3) Early secondary minerals, which are often subhedral to anhedral, occur rimming (Figs. 5d and 6d-e)
241 or enclosing resorbed crystals of the primary phases (sometimes even developing euhedral habits in the
242 interstitial spaces; Fig. 5c), but also form isolated crystals in the groundmass (Fig. 6f). They show highly
243 variable grain sizes, ranging from coarse- to fine-grained (>2 cm to 1 mm). Bertossaite, F-poor montebrasite,
244 scorzalite, augelite, and brazilianite are representatives of early secondary phases, as well as quartz.

245 4) Late secondary minerals are the most diverse group in number of phases present. These minerals are
246 dominantly fine-grained (up to 1 mm) and replace all earlier mineral phases. They often occur as aggregates
247 in pseudomorphs (Fig. 5e) and show complex replacement textures even within the group itself. Euhedral
248 crystals are commonly observed (Fig. 5f), but fine-grained crystal masses are also present. Eosphorite,
249 samuelsonite, hydroxylapatite, burangaite, and wardite, which are observed within the mineralized

assemblages, are highlighted from this group. Although other minerals might be present, a complete sequence of minerals within this group is outside the scope of this study since these phases post-date the Nb-Ta mineralization.

4.1.1.2. *Ore minerals.* Phosphatic nodules contain two Nb-Ta-oxide minerals: 1) Fe-Nb-Ta-rich rutile and 2) a solid solution of the columbite-group minerals (CGM). Rutile is the most common Nb-Ta-bearing phase in the phosphatic nodules. It is euhedral to anhedral and occurs as very-fine inclusions (≤1 mm) in many phases, from the early primary minerals (e.g., wyllieite, Fig. 7a) to some secondary phases (e.g., augelite). In most cases, it is mainly black and opaque under the polarizing microscope, but it can rarely have translucent light brown-reddish colors. In backscattered electron (BSE) images, rutile crystals show concentric oscillatory zoning (Fig. 7b), alternating darker and brighter BSE zones. Nevertheless, many crystals display partially resorbed darker cores directly overgrown by bright rims (upper region of crystal in Fig. 7c), while irregular patches that crosscut the concentric zones are also present (lower part of crystal in Fig. 7c).

CGM are more restricted in the phosphatic nodules, and relatively more frequent in the strongly altered group. They are anhedral, normally associated with altered phosphates, mostly bertossaite and rosemaryite, and have complex zoning textures. The zonation can occasionally be concentric and oscillatory, but often shows disordered patterns with brighter and darker BSE domains unevenly distributed (Fig. 7d and e), and it can have irregular patches cutting the previous domains.

A different texture from all other crystals is seldom observed, with anhedral, oscillatory-zoned rutile directly associated with anhedral homogeneous CGM (Fig. 7f). The CGM seems to partially penetrate the rutile host and even follows an irregular patch cross-cutting the concentric zones, slightly resembling a fracture (note the right side of Fig. 7f).

4.1.2. Albitized facies. This facies is dominated by silicates, with albite by far the most abundant mineral. Samples commonly show isotropic fabric, are white to cream-colored, and have crystal sizes varying from coarse- to fine-grained. Frequent circular reddish oxidation spots and fractures contain opaque oxide-hydroxide minerals. The albitized facies contains only CGM as a Nb-Ta-oxide phase. CGM are texturally homogeneous, showing subhedral to anhedral crystals with signs of partial resorption such as rounded edges. Crystals are mostly unzoned in BSE images, occasionally with slightly brighter rims (Fig. 7g-i). CGM crystals commonly occur as inclusions in albite, as isolated crystals in the albite-quartz groundmass, or rarely associated with other minerals (e.g., zircon and micas).

4.2. Mineral chemistry

Wavelength-dispersive X-ray spectroscopy (WDS) analyses representative of each textural context in the NTO minerals from the Buranga dike are presented in Table 1. The complete dataset for the mineral analyses can be found in the supplementary materials S2.

4.2.1. Rutile. The zonation observed in the rutile crystals is well correlated with chemical variation in their composition. There is a tendency of an increasing Nb+Ta+Fe content towards the rim of the crystals, combined with a decrease in the Ti content (Fig. 8), which indicates that the main cationic exchange observed (Fig. 8a) is the rutile-type substitution: $2(Nb,Ta)^{5+} + Fe^{2+} = 3\ Ti^{4+}$ (Ercit 1994).

The distinction between the partially and strongly altered groups is not clear, with considerable overlap among the phosphatic nodules (Fig. 8b, and Fig. 9a, b, c). However, slightly more Fe-Nb-Ta-rich rutile compositions were observed in the strongly altered nodules (Fig. 9a). This Fe-Nb-Ta-rich character is highlighted in the grains associated with CGM (Fig. 7f), which have an average chemical formula $Ti_{8.85}Fe_{1.22}Nb_{0.99}Ta_{0.88}Sn_{0.14}O_{24}$, showing the highest contents of Nb, Ta, and Fe observed in this study.

294 **4.2.2. Columbite-group minerals.** The chemical compositions of CGM show clear trends and allow
295 discrimination between the studied facies in the Buranga pegmatite (Fig. 8c and d). Contents of Ti and Sn are
296 positively correlated and have the highest values associated with CGM in the phosphatic nodules (Fig. 9d),
297 while the albitized facies shows rather constant low values (commonly lower than 0.2 apfu for Ti+Sn).
298 Oppositely, Nb and Ta are negatively correlated, as well as Fe and Mn, as is expected from the main cationic
299 substitutions that define the group end-members (Černý et al. 1986). For the Ta# (Ta/Ta+Nb) and Mn#
300 (Mn/Mn+Fe) (atomic ratios) indices (Fig. 8d), the partially altered phosphatic nodules have higher Ta# and
301 lower Mn# (average of 36 and 37, respectively) than the strongly altered nodules (17 and 46, respectively).
302 The albitized facies has low Ta# and variable Mn# values (14 and 25), with crystal rims showing a slight
303 increase in the Ta# values (from about 11 in the cores to 18 in the rims).
304 A comparison of the distinct groups shows that Ti is positively correlated with Fe and Ta in the
305 phosphatic nodules, while negatively correlated with Mn and Nb (Fig. 9e and f). Since the Ti content is
306 predominantly low in the albitized facies, it does not change with varying amounts of other cations.
307 The chemical composition is mostly unrelated to any specific location in the crystals (Fig. 9). Usually,
308 cores demonstrate lower Ta contents ($Fe_{2.0}Mn_{1.7}Nb_{6.7}Ta_{1.1}Ti_{0.4}Sn_{0.1}O_{24}$) than their respective rims
309 ($Fe_{2.1}Mn_{1.4}Nb_{5.9}Ta_{2.0}Ti_{0.2}Sn_{0.1}O_{24}$). Nonetheless, few crystals have the opposite behavior of core
310 ($Fe_{2.3}Mn_{1.2}Nb_{4.5}Ta_{3.1}Ti_{0.6}Sn_{0.1}O_{24}$) versus rim ($Fe_{2.2}Mn_{1.4}Nb_{5.6}Ta_{2.2}Ti_{0.4}O_{24}$), and there is considerable overlap
311 between core and rim analyses of different crystals (Fig. 9e and f). Additionally, whenever patchy textures
312 are present in BSE images, usually cross-cutting the other zones, these areas tend to have lower values of
313 Ti+Sn, and Ta# ($Fe_{1.6}Mn_{1.9}Nb_{7.5}Ta_{0.5}Ti_{0.2}O_{24}$) than the other zones (Fig. 10).

314 **4.3. Raman analysis**

315 Raman analysis was used as complementary identification of the observed minerals. The raw and
316 processed spectra for all minerals can be found in the supplementary materials S3 and S4, respectively.

317 **4.3.1. Rutile.** The main Raman modes of the rutile structure are identified as: (1) symmetric bending
318 (E_g) at around 440 cm^{-1}, (2) symmetric stretching (A_{1g}) at around 610 cm^{-1}, (3) asymmetric stretching (B_{1g}) at
319 around 140 cm^{-1}, and (4) asymmetric stretching (B_{2g}) at around 810 cm^{-1} (Porto et al. 1967).

320 These normal modes are straightforwardly recognized in the spectra of the crystals that show high Ti
321 contents (Fig. 11a), while they become less distinct in spectra of crystals that have higher Nb+Ta+Fe
322 contents, which also show broader Raman peaks (Fig. 11b). The darker crystal zones in BSE images (usually
323 the crystal cores - Fig. 7) have narrower Raman peaks for which the positions directly correspond to the
324 position based on the pure Raman spectrum of rutile (Porto et al. 1967), and are considered here as normal
325 spectra. Bright BSE zones (especially the crystal rims) show slightly shifted and broader Raman peaks, in
326 combination with more Raman peaks than the theoretical rutile Raman spectrum, and are considered as
327 disturbed spectra.

328 A small shift in the position of the E_g and A_{1g} bands is visible in the disturbed spectra, changing from
329 around 440 and 610 cm^{-1} to 410 and 625 cm^{-1}, respectively. This means that the distance between the two
330 main peaks (E_g and A_{1g} bands) increases with increasing Nb+Ta+Fe content. The intensity of the peak at
331 around 840 cm^{-1} also significantly increases in the disturbed spectra, which might be related to a stronger
332 influence of (Nb,Ta)-O vibrations (Moreira et al. 2010), as can be seen in the CGM spectra (Fig. 12).

333 **4.3.2. Columbite-group minerals.** The Raman spectra of CGM do not show many differences in
334 relationship with the chemical composition, textural contexts, or facies (Fig. 12). Band assignments presented
335 below are after the studies of Husson et al. (1977) and Moreira et al. (2010). The spectra are marked by a
336 strong vibration at around 880 cm^{-1}, which is assigned as the $(Nb,Ta)O_6$ octahedron symmetric stretching
337 vibration (A_{1g}). Other distinct modes are present at 635, 532, 395 cm^{-1} assigned to (NbTa)-O bond vibrations,
338 and at around 275 cm^{-1} assigned as stretching vibrations of the (Fe,Mn)-O bonds. Several less intense and
339 overlapping modes can be further observed, where the ones below 250 are related to lattice vibrations,
340 between 250-380 cm^{-1} are assigned as octahedra bending coupled with (Fe,Mn)–O stretching, and remaining
341 modes due to the (Nb,Ta)-O vibrations.
342
343 **4.3.3. Host minerals.** NTO are associated with both primary and secondary minerals as discussed in
344 section 4.1. The spatial characterization of those is not always easy by petrographic microscopy, SEM, or
345 EPMA, but they can be unambiguously identified by Raman mapping (Araujo et al. 2021). Raman maps are
346 hyperspectral images with vibrational data of the region of interest and can show molecular changes at
347 micrometer scales.
348 Raman maps show that rutile and wyllieite are not affected by the replacement of the surrounding
349 trolleite by F-poor montebrasite (Fig. 13). Consequently, this alteration post-dates rutile precipitation.
350 When the rutile crystals are isolated in the groundmass, i.e., they are not locked as inclusions in other
351 phases, they are more susceptible to alteration processes. The mixed rutile-CGM grain (Fig. 14a) illustrates
352 this relationship between rutile alteration and its host phosphate (Fig. 14b). In this assemblage, the trolleite
353 host locally shows bands at around 975, 987, 1022, and 1041 cm^{-1}. These uncommon bands are absent in the
354 trolleite spectrum (Araujo et al. 2021) and are correlated with bands from brazilianite (complete set of spectra
355 available in the supplementary files). The location showing the highest intensity for the brazilianite signal
356 (brightest pixels at the left bottom of Fig. 14c) is associated with the CGM occurrence (Fig. 14d), whereas
357 the area around the rutile crystal (Fig. 14e) correlates to the trolleite signal (Fig. 14f).

This is the peer-reviewed, final accepted version for American Mineralogist, published by the Mineralogical Society of America.
The published version is subject to change. Cite as Authors (Year) Title. American Mineralogist, in press.
DOI: https://doi.org/10.2138/am-2022-8201. http://www.minsocam.org/

CGM crystals are usually hosted in alteration pods within large phosphate crystals (Fig. 15a). Although the many phases present can be hard to identify under the electron microscope (Fig. 15b), Raman mapping yields a detailed phase image. CGM occurs inside partially altered rosemaryite and is commonly surrounded by bertossaite (Fig. 15c). The rosemaryite crystals themselves are further altered by eosphorite, samuelsonite, hydroxylapatite, whereas scorzalite and wardite can form at the interface with trolleite, but these seem to be unrelated to the CGM precipitation.

5. DISCUSSION

The terminology regarding the terms primary and secondary is based mainly on the textures of the minerals, as described in section 4.1. In most cases, primary minerals are interpreted as early to late phases that precipitate directly from the medium (in this case the melt) due to oversaturation, whereas secondary minerals represent overprinting or replacement phases, which crystallize due to reactions between earlier minerals and the crystallizing medium (either a melt or a fluid). The purpose of this discussion is to assess in which stage of the dike formation the phosphate minerals, and the NTO, have crystallized, and thus interpret the processes that could trigger the mineralization.

5.1. From mineral paragenesis to crystallization stages

Phosphate minerals crystallize at multiple stages in the phosphorus-rich Buranga rare-element pegmatite (Fig. 4), and rutile or CGM are each associated with distinct phosphate assemblages. Mineral assemblages in the phosphatic nodules are divided as (1) early primary (rutile, wyllieite, F-rich montebrasite, fluorapatite, and rosemaryite), (2) late primary (trolleite, muscovite, and quartz), (3) early secondary (CGM, bertossaite, F-poor montebrasite, scorzalite, augelite, brazilianite, and quartz), and (4) late secondary (eosphorite, samuelsonite, hydroxylapatite, burangaite, and wardite). In the albitization facies, an early (tourmaline, beryl, zircon, fluorapatite, eosphorite) and a late (CGM, albite, muscovite, quartz) assemblage are observed. In the more general paragenesis proposed for the Gitarama-Gatumba pegmatite field based on optical microscopy (Dewaele et al. 2011), the Nb-Ta mineralization is placed within the broad ‘magmatic stage’ (‘pegmatite intrusion’) alongside the general precipitation of phosphate minerals. However, the detailed paragenesis from

this study demonstrates that the NTO mineralization takes place in more than one stage. Furthermore, the diverse phosphate mineralogy can be used to identify the detailed settings in which Nb-Ta oxide mineralization occurred.

Textural relations of phosphate minerals in the Buranga dike (Figs. 5, 6, and 15) suggest that the early minerals (F-rich montebrasite, wyllieite, fluorapatite, and rosemaryite), which occur as resorbed coarse-grained crystals or as euhedral inclusions in later phases and show a lack of fluid inclusions, precipitated directly from the melt. Therefore, they are classified as the magmatic minerals in the sequence, as is observed in other rare-element pegmatites (e.g., London and Burt 1982).

Regarding the late primary and early secondary minerals (i.e., trolleite, bertossaite, F-poor montebrasite, scorzalite, augelite, and brazilianite), the textures are slightly ambiguous concerning the precipitation conditions. The occurrence of coarse-grained crystals, sometimes with interstitial aspect and enclosing previous phases (Figs. 5b and d, 6c, and 15) point to a magmatic origin. Conversely, the occurrence of early secondary minerals surrounding resorbed primary phases (Figs. 5c and 6d-e) suggests a partial dissolution of the latter, followed by precipitation of the former, which could happen either in a residual melt or a fluid medium. Nonetheless, although ambiguous to the medium, the textures point to physical disruption of the primary minerals, but without signs of pervasive pseudomorphic replacement as it is observed with the late secondary phosphates (Fig. 5e) in subsolidus processes (fluid-crystal reaction). In this stage, primary crystals are broken up but not intensively replaced, and early secondary minerals precipitate in the open spaces rather than at the expense of previous phases. Furthermore, considering the composition of those minerals, it is not expected that all the required components (Al, P, Ca, Na, Si, Fe, and Si) are provided only by the fluid (London et al. 1988; Keppler 1994), nor that a massive coarse-grained crystal (with brecciated/poikilitic-like textures) would precipitate from subsolidus processes. Therefore, on the one hand, it is likely that a residual melt was present during this stage. On the other hand, the widespread presence of primary fluid inclusions in all these minerals suggests that a fluid phase was also present during crystallization. Considering the

combined evidence of magmatic textures with frequent primary fluid inclusions, these minerals are interpreted to have crystallized from a medium where both melt and fluid coexisted.

Finally, the late secondary minerals, which often occur as fine-grained euhedral crystals or aggregates inside fractures and in pseudomorphs after the primary minerals (Fig. 5e and f), indicate mostly fluid-related processes in a subsolidus setting. Therefore, they are interpreted as precipitating after complete crystallization from reactions between the previous phases and the fluid.

5.1.1. Key assemblages hosting ore minerals. Rosemaryite was previously described as being too oxidized to be a primary phase (Fransolet 1995). Some authors propose that wyllieite is the common primary mineral and that rosemaryite forms by its oxidation (Fransolet 1995; Hatert et al. 2016). However, in the Al-rich phosphatic nodules, rosemaryite occurs as inclusions in trolleite, augelite, quartz, and brazilianite, equally as wyllieite. Additionally, there are no indications of a direct relationship between the two, neither as relics of wyllieite inside rosemaryite nor as signs of replacement of the former by the latter to confirm this oxidation reaction, a feature also highlighted by Fransolet (1995). Moreover, these two minerals occur as spatially close inclusions inside F-poor montebrasite, trolleite, and augelite. Those findings suggest a primary character for both phosphates. The occurrence of oxidized primary Fe-Mn phosphates and oxides has already been described in the Buranga dike (Fransolet 1975) and other phosphorus-rich pegmatites (Roda et al. 2004; Roda-Robles et al. 2020), and in experimental studies (Hatert et al. 2006, 2011a), suggesting that an increased fO_2 of the melt enables crystallization of such phases. In the same way, both wyllieite and rosemaryite are interpreted as primary phosphates. Wyllieite crystallizes earlier at lower melt fO_2 conditions, while rosemaryite is stabilized later when the melt becomes slightly more oxidized.

Overall, rutile is observed when both wyllieite and rosemaryite occur in the assemblage. Conversely, CGM is present in the assemblages that showed only altered rosemaryite and no wyllieite, or where both phosphates were completely replaced. Therefore, rutile formation does not seem to depend on the occurrence or absence of any other phase. This, in addition to the fact that rutile occurs as inclusions in a variety of minerals, even primary phosphates, indicates that rutile crystallization started early in the phosphatic nodules.

Contrarily, CGM crystals are paragenetically linked with the formation of secondary phosphates. CGM commonly occur associated with bertossaite, either together in alteration nests within rosemaryite in the partially altered phosphatic nodules, or as inclusions of CGM in bertossaite in the strongly altered nodules. Bertossaite is mostly present as an alteration of montebrasite and trolleite but also occurs as inclusions in the latter. This indicates that the formation of bertossaite is not straightforward and should be interpreted with care since it could be stable in multiple stages and under variable conditions, possibly due to its structure being able to host multiple components (e.g., Li, Na, Ca, Sr, Al, Fe, Mn; Hatert et al., 2011b). In any case, bertossaite and CGM crystallization occur between the onset of the chemical remobilization by a fluid phase under magmatic conditions and the complete solidification of the dike. The formation of CGM in the phosphatic nodules seems to depend on the destabilization of wyllieite, rutile, and rosemaryite, and the crystallization of bertossaite.

Additionally, the absence of complex NTO associations (multiple secondary Ta-bearing oxides as seen in Van Lichtervelde et al., 2007) indicates that CGM crystals did not react with the residual melt or the exsolved fluid (as it happened with the primary phosphates). This reinforces the idea that CGM crystallized from a medium that was in disequilibrium with the primary phosphates (i.e., residual melt + fluid), and that they precipitated all at once in the late stage.

448 **5.1.2. Crystallization stages.** To explain the observed mineral textures and their respective sequences
449 (Figs. 4, 5, 6, 7, 14, 15, 16), the following processes are proposed for the crystallization of Buranga's
450 phosphatic nodules. Initially, at the magmatic stage, Li-rich and anhydrous minerals precipitate from the melt
451 (e.g., F-rich montebrasite, wyllieite, fluorapatite, and rosemaryite). Subsequently, hydrated phases (i.e.,
452 trolleite) are precipitated and fluid inclusions become a common feature. This marks the magmatic-
453 hydrothermal stage, where a high-temperature fluid is exsolved from the melt. At this stage, where crystal,
454 melt, and fluid coexist, the fluid phase reacts with the primary minerals and redistributes some of their
455 components to the residual melt, leading to the formation of phases with mobile elements such as Ca, Na, and
456 Fe (Mn) (e.g., bertossaite, scorzalite-lazulite, and brazilianite). Finally, after the complete crystallization,
457 intense hydration is the dominant process, stabilizing minerals with molecular water in the crystal structure
458 (e.g., childrenite-eosphorite, samuelsonite, wardite, hydroxylapatite, burangaite) at the hydrothermal stage.
459 This indicates that an aqueous fluid was still available at subsolidus conditions, partly remobilizing the more
460 fluid-mobile elements and extensively altering the previous minerals.

461 Textural groups observed in this study (section 4.1) can be reclassified into the crystallization stages: 1)
462 magmatic, with crystallization of primary phases directly from the melt, 2) magmatic-hydrothermal, where
463 late primary and early secondary phases crystallize due to crystal-melt-fluid interactions, and 3)
464 hydrothermal, where late secondary phases are formed by replacement of earlier phosphates under subsolidus
465 conditions in the presence of an aqueous fluid (Fig. 16).

466 From the three stages described above for the Al-rich phosphatic nodules in the Buranga dike, rutile
467 precipitation is associated with the crystallization of primary minerals (F-rich montebrasite, wyllieite,
468 fluorapatite, and rosemaryite) at the magmatic stage, whereas CGM precipitation occurs concomitantly to the
469 crystallization of early secondary phosphates (especially bertossaite) after the alteration of primary minerals
470 during the magmatic-hydrothermal stage. Nevertheless, this information is not sufficient to understand the
471 cause of NTO oversaturation and mineralization at each respective stage.

472 **5.2. Precipitation of rutile and columbite-group minerals**

This is the peer-reviewed, final accepted version for American Mineralogist, published by the Mineralogical Society of America.
The published version is subject to change. Cite as Authors (Year) Title. American Mineralogist, in press.
DOI: https://doi.org/10.2138/am-2022-8201. http://www.minsocam.org/

473 **5.2.1. Rutile.** Rutile is typically a magmatic phase in rare-element pegmatites (Abella et al. 1995;
474 Ballouard et al. 2020a). Saturation of rutile occurs due to its low solubility in peraluminous hydrous silicic
475 melts (Ryerson and Watson 1987; Kularatne and Audétat 2014) and can be enhanced by the local
476 concentration of Ti at the crystal-liquid interface (melt boundary layers) of crystallizing primary phosphates
477 (cf. Bacon 1989), where high field strength elements (HFSE) are incompatible elements. The melt Nb and Ta
478 content would also gradually increase at these crystal-liquid interfaces (London 2018), and both metals could
479 enter the rutile structure (Linnen and Keppler 1997; Linnen and Cuney 2005).

480 Experiments indicate that rutile preferably incorporates Nb over Ta, with a higher partition coefficient
481 ($D_{rutile/melt}$) for Nb than for Ta in granitic melts: $D^{Nb}/D^{Ta} = 2.6$ (Linnen and Keppler 1997; Linnen and Cuney
482 2005). Consequently, a consistent change in the melt Nb/Ta ratio would be expected with rutile precipitation
483 in an equilibrium fractional crystallization model without the precipitation of any other NTO. This behavior
484 is not observed in the crystals analyzed in this study (Fig. 9c). The investigated rutile crystals show a general
485 trend of Nb+Ta+Fe enrichment with crystallization, but without a regular Nb/Ta change since core and rim
486 analyses of different crystals irregularly overlap.

487 The higher Nb+Ta+Fe contents and irregular Nb/Ta distribution coupled with the stronger
488 crystallographic disorder towards the rims of the rutile crystals (Fig. 11b) indicate that rutile precipitation did
489 not follow an equilibrium path. The occurrence of resorbed cores (Fig. 7c) also hints that the Ti-rich phases
490 were unstable and in disequilibrium with the late magmatic residual melt. A possible interpretation is that
491 when rutile remained in contact with the residual melt, it was partially resorbed. Subsequently, with HFSE
492 still available in the melt, rutile followed a disequilibrium crystallization path. Local supersaturation at the
493 crystal-liquid interfaces was possibly what generated the oscillatory zoning and Fe-Nb-Ta-rich rims (Beurlen
494 et al. 2008; Van Lichtervelde et al. 2018; Ballouard et al. 2020a; Kaeter et al. 2021). Chemical quenching at
495 the crystal-liquid interfaces due to consumption of P and Li (crystallization of phosphates) can also enhance
496 this supersaturation, leading to a quick crystallization of rutile, as suggested by Kaeter et al. (2021) in the
497 case of tourmaline and Nb-Ta-rich rutile association.

498 **5.2.2. Columbite-group minerals.** Contrarily to rutile, columbite-group minerals (CGM) are not
499 widespread in the phosphatic nodules and occur only within alteration pods in primary phosphates (Fig. 15).
500 This association suggests that CGM crystallization was not caused by supersaturation in the melt, but was
501 rather triggered by the destabilization of primary phases at the magmatic-hydrothermal stage (Fig. 16).

502 Considering the partially altered phosphatic nodules, only the areas close to extensive brazilianite
503 formation show CGM in the pseudomorphs after rosemaryite. This could indicate that although brazilianite
504 has not been seen in direct association with ore minerals, Na-metasomatism plays a role in the CGM
505 precipitation. This influence is directly visible in the rutile + CGM coupled crystal (Fig. 14). Alternatively,
506 the spatial correlation could simply be due to high permeability zones that concentrate most metasomatic
507 processes, explaining the formation of brazilianite close to the rosemaryite pseudomorphs. However, many
508 regions are altered by other secondary phases (e.g., augelite, scorzalite, and hydroxylapatite) and only show
509 rutile. Furthermore, Na-metasomatism has already been evoked as the main trigger for Nb-Ta mineralization
510 in pegmatites (Kontak 2006) and can explain the occurrence of exclusively CGM in the albitization facies.
511 Indeed, Fransolet (1975) reported that Na-metasomatism in the phosphatic nodules is concomitant with the
512 albitization of silicate minerals.

513 The low Nb-Ta content of exsolved magmatic fluids, as has been deduced from fluid inclusion research
514 (Zajacz et al. 2008; Borisova et al. 2012), low fluid/melt partition coefficients (London et al. 1988; Borodulin
515 et al. 2009; Tang and Zhang 2015), and consequently, low mobilization of Nb-Ta by fluids (Linnen and
516 Cuney 2005), need to be overcome to explain the precipitation of CGM in a magmatic-hydrothermal stage.
517 The key is that GCM precipitation requires not only Nb and Ta but also Fe and Mn (Linnen and Keppler
518 1997). Considering that Fe and Mn are more mobile than Nb and Ta (Zajacz et al. 2008), the remobilization
519 of Fe-Mn by saline fluids into a Nb-Ta-bearing residual melt can precipitate CGM (McNeil et al. 2020).

520 The crystallization of phosphates should decrease the availability of Fe and Mn in the melt, similarly to
521 the early crystallization of Fe-Mn-Mg-bearing silicates like biotite or schorl-dravite tourmaline (London et al.
522 1999; Roda-Robles et al. 2012; McNeil et al. 2020), increasing the solubility of CGM (Linnen and Keppler

523 1997; McNeil et al. 2020). Phosphates compete with CGM for the Fe-Mn content in the melt and, due to the
524 P-rich nature of the melt, phosphates are preferentially crystallized. This means that CGM can only
525 precipitate after the primary phosphates are altered and the Fe-Mn content previously locked in their structure
526 becomes available. The textures observed (fractured crystals, rim aureoles, primary fluid inclusions, etc.) are
527 more indicative of a reaction between the primary phosphates and a fluid phase in the crystal-melt-fluid
528 system, but the involvement of the residual melt in reactions with the phosphates cannot be completely ruled
529 out.

530 Nonetheless, if the Fe and Mn content in the melt is not sufficient to precipitate CGM, Nb and Ta stay in
531 the melt at the magmatic-hydrothermal stage until Fe and Mn are made available (Linnen and Keppler 1997;
532 McNeil et al. 2020). The reaction of the exsolved fluid with Fe-Mn-bearing sources (country rock or, in this
533 case, primary phosphates) can then remobilize the fluid-mobile elements like Fe-Mn-Ca from the primary
534 minerals back into the melt and trigger the CGM precipitation.

535 For this reason, a magmatic-hydrothermal origin (melt-fluid-crystal interaction) is preferred over a melt-
536 melt immiscibility origin. At the magmatic-hydrothermal stage, the three required components are present
537 (Nb-Ta-bearing residual melt + exsolved fluid + Fe-Mn primary phosphates). The exsolved fluid reacts with
538 the primary phosphates, releasing Fe and Mn to the environment. Subsequently, the newly available Fe and
539 Mn can combine with the Nb and Ta from the residual melt to precipitate CGM. Contrarily, at a pure
540 magmatic stage with melt-melt immiscibility, it is not expected that the primary phosphates are in
541 disequilibrium with the residual melts and would thus not be dissolved to release Fe and Mn back to the melt.

542 The requirement of Fe and Mn to precipitate CGM can also explain the lack of NTO in the Fe-Mn-rich
543 nodules since the Fe and Mn content is locked in the phosphates during the whole crystallization. Even when
544 primary phases are altered, the secondary phases are still Fe-Mn-rich, obstructing the precipitation of CGM.
545 Contrarily, in the Al-rich nodules, after the alteration of the primary Fe-Mn-bearing phosphates (e.g.,
546 rosemaryite and wyllieite), the secondary phosphates are mainly Al-rich (e.g., bertossaite, brazilianite). Thus,
547 Fe and Mn are available in the system, and CGM can precipitate.

548 The chemical trends between the partially and strongly altered nodules (Figs. 8 and 9) suggest that weak
549 alteration releases more Fe and Ta, and as the alteration progresses, more Mn and Nb are remobilized. The
550 alteration patterns reflect a more favorable composition in the strongly altered nodules (i.e., a larger presence
551 of muscovite or other "reactive" minerals). This suggests that crystal-melt-fluid reactions and precipitation of
552 CGM are local events rather than homogeneously distributed through the pegmatite body. Consequently, the
553 dike system was not in equilibrium as a whole, and distinct, localized evolutions occurred for Al-rich and Fe-
554 Mn-rich nodules, with each nodule acting as a separated chemical system. A similar local disequilibrium
555 crystallization has already been described for the multi-stage cassiterite mineralization in the Gatumba dike
556 system (Hulsbosch and Muchez 2020), nearby the Buranga dike.

557 Finally, some of the Nb-Ta content from the residual melt could have been mobilized to precipitate
558 CGM in the albitized facies. Although the fluid-melt partitions of Nb and Ta ($D_{Ta}^{fluid/melt} < 0.008$ and D_{Nb}^{fluid-}
559 $^{melt} < 0.022$, Borodulin et al. 2009) are considerably low in peraluminous melts (Chevychelov et al. 2010),
560 they can be soluble in concentrated acidic fluoride solutions (Zaraisky et al. 2010; Akinfiev et al. 2020), with
561 Nb having slightly lower solubility than Ta (Timofeev et al. 2015), and could thus be partially remobilized by
562 fluids. Fluid-mediated mobilization and precipitation for CGM is commonly described in alkaline granitoids
563 and pegmatites (Timofeev and Williams-Jones 2015; Siachoque et al. 2020) and should be related to the high
564 Na and F content of the exsolved fluids. However, the lack of fluorine phases (e.g., topaz and fluorite), and
565 the F-poor compositions reported for minerals and fluid inclusions in the Gitarama-Gatumba pegmatite field,
566 including the Buranga dike (Hulsbosch 2019; Hulsbosch and Muchez 2020; Araujo et al. 2021), suggest a
567 low fluorine content in the pegmatite system. Consequently, Nb and Ta have not been extensively mobilized
568 by the fluid phase and remained close to the melt source. This indicates that although alkali-rich fluids were
569 responsible for the albitization, the Nb-Ta content was mainly concentrated during the magmatic stage in the
570 Buranga pegmatite and remained in the melt until CGM precipitation.

571 **5.3. Crystallization and mineralization model**

572 Combining all the observations from this study, a mineralization model is proposed for the Buranga
573 pegmatite (Fig. 17): at the magmatic stage, large primary phosphates crystallize and locally increase the
574 HFSE content in the crystal-melt interface (melt boundary layer), triggering rutile precipitation adjacently to
575 these phosphates by local supersaturation. With the progression of crystallization, the melt becomes
576 comparatively enriched in incompatible elements, but the low availability of Fe-Mn in the melt due to the
577 stabilization of primary Fe-Mn-rich phosphates inhibits the saturation of CGM. In this case, Nb and Ta can
578 be concentrated in the residual melt, incorporated in the compatible phase rutile, or dispersed as traces in
579 complex phosphates such as montebrasite, wyllieite, and rosemaryite. At the late magmatic stage, a high-
580 temperature aqueous fluid is exsolved (magmatic-hydrothermal stage) and reacts with the primary phases,
581 dissolving them. The reaction remobilizes Fe and Mn from the phosphates to the residual melt and,
582 consequently, locally precipitates CGM around the altered primary phosphates.
583
584 **6. IMPLICATIONS**
585 The precipitation of niobium-tantalum-oxide minerals (NTO) in the Buranga pegmatite is not only
586 controlled by the availability of HFSE but also by other mineral-forming elements (i.e., Fe and Mn).
587 Consequently, the crystallization and stability of Fe-Mn-rich primary phosphates buffer the formation of
588 NTO in phosphorus-rich rare-element pegmatites, especially for the columbite-group minerals (CGM). The
589 textural and chemical features of NTO do not reflect the general pegmatite fractionation but indicate local
590 processes and instabilities. Fe-Nb-Ta-rich rutile precipitated directly from the melt due to supersaturation in
591 its components. Local disequilibrium between the flux-rich melt and the growing primary phosphates is
592 likely the main cause of rutile crystallization. CGM are formed at the magmatic-hydrothermal stage due to
593 phosphate-melt-fluid interactions, which releases Fe and Mn to the residual melt and locally precipitates
594 CGM. The phosphatic nodules show complex precipitation stages, and each nodule could behave mostly as a
595 separated system, until the very late stages of hydrothermal alteration, where fluids can escape from the
596 system. The textural context of the whole assemblage, not only of single minerals, is particularly important to

reconstruct the crystallization sequences. Accordingly, the rich record from phosphate minerals is a powerful tool to deduce the precipitation conditions of niobium-tantalum-oxide minerals in phosphorus-rich pegmatites, controlling the availability of chemical components and providing a proxy for the mineralization stage.

ACKNOWLEDGEMENTS

Fernando Prado Araujo is funded by a PhD scholarship from KU Leuven. Research of Niels Hulsbosch was supported by an FWO Junior Postdoctoral Fellowship. The Raman equipment was acquired via the medium-scale research infrastructure FWO grant Raman-SIM2 (number I000718N), and the research is financially supported by Research Grant C14/17/056 of the KU Leuven Research Fund. The authors are grateful to Stijn Dewaele (UGent), Florias Mees (Royal Museum for Central Africa), and Frederic Hatert (ULiège) for providing the samples. Herman Nijs (KU Leuven) is thanked for preparing the high-quality thin sections. Valeria Fonseca and Marco Dalla Vecchia are thanked for helping with the python scripts. The help of Luiza Freitas in the edition of the manuscript is much appreciated. Careful reviews and constructive comments of the editor David Dolejš, and reviewers Pavel Uher, and Marieke Van Lichtervelde helped to improve the quality of this manuscript. The first author thanks Robert Linnen, Alysha McNeil, Olivier Namur, Anouk Borst, and Laura van der Does for the discussions about the magmatic-hydrothermal textures.

7. REFERENCES

Abella, P.A., Cordomi, M.C., and Draper, J.-C.M. (1995) Nb-Ta-minerals from the Cap de Creus pegmatite field, eastern Pyrenees: distribution and geochemical trends. Mineralogy and Petrology, 55, 53–69.

Akinfiev, N.N., Korzhinskaya, V.S., Kotova, N.P., Redkin, A.F., and Zotov, A. V. (2020) Niobium and tantalum in hydrothermal fluids: Thermodynamic description of hydroxide and hydroxofluoride complexes. Geochimica et Cosmochimica Acta, 280, 102–115.

Araujo, F.P., Martins, L., Pereira, G. de S., and Janasi, V. de A. (2020) Inhandjara topaz leucogranite: A late rare metal-mineralized stock within the A-type Itu batholith, SE Brazil. Journal of South American

622 Earth Sciences, 101, 102623.

623 Araujo, F.P., Hulsbosch, N., and Muchez, P. (2021) High spatial resolution Raman mapping of complex
624 mineral assemblages: Application on phosphate mineral sequences in pegmatites. Journal of Raman
625 Spectroscopy, 52, 690–708.

626 Armstrong, J.T. (1991) Quantitative elemental analysis of individual microparticles with electron beam
627 instruments. In K.F.J. Heinrich and D.E. Newbury, Eds., Electron Probe Quantitation pp. 261–315.
628 Plenum Press, New York.

629 Bacon, C.R. (1989) Crystallization of accessory phases in magmas by local saturation adjacent to
630 phenocrysts. Geochimica et Cosmochimica Acta, 53, 1055–1066.

631 Baijot, M., Hatert, F., Dal Bo, F., and Philippo, S. (2014) Mineralogy and petrography of phosphate mineral
632 associations from the Jocão pegmatite, Minas Gerais, Brazil. The Canadian Mineralogist, 52, 373–397.

633 Ballouard, C., Elburg, M.A., Tappe, S., Reinke, C., Ueckermann, H., and Doggart, S. (2020a) Magmatic-
634 hydrothermal evolution of rare metal pegmatites from the Mesoproterozoic Orange River pegmatite belt
635 (Namaqualand, South Africa). Ore Geology Reviews, 116, 103252.

636 Ballouard, C., Massuyeau, M., Elburg, M.A., and Tappe, S. (2020b) The magmatic and magmatic-
637 hydrothermal evolution of felsic igneous rocks as seen through Nb-Ta geochemical fractionation, with
638 implications for the origins of rare-metal mineralizations. Earth-Science Reviews, 203, 103115.

639 Bartels, A., Holtz, F., and Linnen, R.L. (2010) Solubility of manganotantalite and manganocolumbite in
640 pegmatitic melts. American Mineralogist, 95, 537–544.

641 Bass, J.D., and Sclar, C.B. (1979) The stability of trolleite and the Al_2O_3-$AlPO_4$-H_2O phase diagram.
642 American Mineralogist, 64, 1175–1183.

643 Beurlen, H., Silva, M.R.R., Thomas, R., Soares, D.R., and Olivier, P. (2008) Nb-Ta-(Ti-Sn) oxide mineral
644 chemistry as tracer of rare-element granitic pegmatite fractionation in the Borborema Province,
645 Northeastern Brazil. Mineralium Deposita, 43, 207–228.

646 Borisova, A.Y., Thomas, R., Salvi, S., Candaudap, F., Lanzanova, A., and Chmeleff, J. (2012) Tin and

associated metal and metalloid geochemistry by femtosecond LA-ICP-QMS microanalysis of pegmatite–leucogranite melt and fluid inclusions: new evidence for melt–melt–fluid immiscibility. Mineralogical Magazine, 76, 91–113.

Borodulin, G.P., Chevychelov, V.Y., and Zaraysky, G.P. (2009) Experimental study of partitioning of tantalum, niobium, manganese, and fluorine between aqueous fluoride fluid and granitic and alkaline melts. Doklady Earth Sciences, 427, 868–873.

Černý, P., and Ercit, T.S. (1985) Some recent advances in the mineralogy and geochemistry of Nb and Ta in rare-element granitic pegmatites. Bulletin de Mineralogie, 108, 499–532.

Černý, P., Meintzer, R.E., and Anderson, A.J. (1985) Extreme fractionation in rare-element granitic pegmatites: selected examples of data and mechanisms. The Canadian Mineralogist, 23, 381–421.

Černý, P., Goad, B.E., Hawthorne, F.C., and Chapman, R. (1986) Fractionation trends of the Nb- and Ta-bearing oxide minerals in the Greer Lake pegmatitic granite and its pegmatite aureole, southeastern Manitoba. American Mineralogist, 71, 501–517.

Černý, P., Chapman, R., Ferreira, K., and Smeds, S.-A. (2004) Geochemistry of oxide minerals of Nb, Ta, Sn, and Sb in the Varutrask granitic pegmatite, Sweden: The case of an "anomalous"columbite-tantalite trend. American Mineralogist, 89, 505–518.

Chevychelov, V.Y., Borodulin, G.P., and Zaraisky, G.P. (2010) Solubility of columbite, (Mn, Fe)(Nb, Ta)2O6, in granitoid and alkaline melts at 650-850°C and 30-400 MPa: An experimental investigation. Geochemistry International, 48, 456–464.

Daltry, V.D.C., and von Knorring, O. (1998) Type-mineralogy of Rwanda with particular reference to the Buranga pegmatite. Geologica Belgica, 1, 9–15.

De Clercq, S., Chew, D., O'Sullivan, G., De Putter, T., De Grave, J., and Dewaele, S. (2021) Characterisation and geodynamic setting of the 1 Ga granitoids of the Karagwe-Ankole belt (KAB), Rwanda. Precambrian Research, 356, 106124.

Dewaele, S., Henjes-Kunst, F., Melcher, F., Sitnikova, M., Burgess, R., Gerdes, A., Fernandez-Alonso, M.,

de Clercq, F., Muchez, P., and Lehmann, B. (2011) Late Neoproterozoic overprinting of the cassiterite and columbite-tantalite bearing pegmatites of the Gatumba area, Rwanda (Central Africa). Journal of African Earth Sciences, 61, 10–26.

Ercit, T.S. (1994) The geochemistry and crystal chemistry of columbite-group minerals from granitic pegmatites, Southwestern Greenville Province, Canadian Shield. The Canadian Mineralogist, 32, 421–438.

Fernandez-Alonso, M., Laghmouch, M., Tack, L., and Tahon, A. (2007) Geological map of the Mesoproterozoic Northeastern Kibara Belt. Tervuren (Belgium).

Fernandez-Alonso, M., Cutten, H., De Waele, B., Tack, L., Tahon, A., Baudet, D., and Barritt, S.D. (2012) The Mesoproterozoic Karagwe-Ankole Belt (formerly the NE Kibara Belt): The result of prolonged extensional intracratonic basin development punctuated by two short-lived far-field compressional events. Precambrian Research, 216–219, 63–86.

Fiege, A., Simon, A.C., Linsler, S.A., Bartels, A., and Linnen, R.L. (2018) Experimental constraints on the effect of phosphorous and boron on Nb and Ta ore formation. Ore Geology Reviews, 94, 383–395.

Fisher, D.J. (1958) Pegmatite phosphates and their problems. American Mineralogist, 43, 181–207.

Fransolet, A.-M. (1975) Etude minéralogique et pétrologique des phosphates de pegmatites granitiques. Fascicule I: Texte. 333 p. Ph.D. thesis, University of Liège, Liège. (in French).

——— (1980) The eosphorite-childrenite series associated with the Li-Mn-Fe phosphate minerals from the Buranga pegmatite, Rwanda. Mineralogical Magazine, 43, 1015–1023.

——— (1995) Wyllieite et rosemaryite dans la pegmatite de Buranga, Rwanda. European Journal of Mineralogy, 7, 567-576. (in French).

Fuchsloch, W.C., Nex, P.A.M., and Kinnaird, J.A. (2019) The geochemical evolution of Nb–Ta–Sn oxides from pegmatites of the Cape Cross–Uis pegmatite belt, Namibia. Mineralogical Magazine, 83, 161–179.

Galliski, M.Á., Černý, P., Márquez-Zavalía, M.F., and Chapman, R. (2012) An association of secondary Al-Li-Be-Ca-Sr phosphates in the San Elías pegmatite, San Luis, Argentina. The Canadian Mineralogist,

50, 933–942.

Galliski, M.Á., Márquez-Zavalía, M.F., Škoda, R., Novák, M., Čopjaková, R., and Pagano, D.S. (2019) A Ta,Ti–rich oxide mineral assemblage from the Nancy beryl–columbite–phosphate granitic pegmatite, San Luis, Argentina. Mineralogy and Petrology, 113, 687–701.

Green, T.H. (1995) Significance of Nb/Ta as an indicator of geochemical processes in the crust-mantle system. Chemical Geology, 120, 347–359.

Hatert, F., Fransolet, A.-M., and Maresch, W. V. (2006) The stability of primary alluaudites in granitic pegmatites: an experimental investigation of the $Na_2(Mn_{2-2x}\ Fe_{1+2x})(PO_4)_3$ system. Contributions to Mineralogy and Petrology, 152, 399–419.

Hatert, F., Ottolini, L., and Schmid-Beurmann, P. (2011a) Experimental investigation of the alluaudite + triphylite assemblage, and development of the Na-in-triphylite geothermometer: Applications to natural pegmatite phosphates. Contributions to Mineralogy and Petrology, 161, 531–546.

Hatert, F., Lefevre, P., and Fransolet, A.-M. (2011b) The crystal structure of bertossaite, $CaLi_2[Al_4(PO_4)_4(OH,F)_4]$. The Canadian Mineralogist, 49, 1079–1087.

Hatert, F., Galliski, M.Á., Roda-Robles, E., Vignola, P., and Fransolet, A.-M. (2016) Crystal chemistry of the wyllieite group of phosphate minerals. The Canadian Mineralogist, 54, 1087–1101.

Hulsbosch, N. (2019) Nb-Ta-Sn-W Distribution in Granite-related Ore Systems. In S. Decrée and L.J. Robb, Eds., Ore Deposits: Origin, Exploration, and Exploitation pp. 75–107.

Hulsbosch, N., and Muchez, P. (2020) Tracing fluid saturation during pegmatite differentiation by studying the fluid inclusion evolution and multiphase cassiterite mineralisation of the Gatumba pegmatite dyke system (NW Rwanda). Lithos, 354–355, 105285.

Hulsbosch, N., Hertogen, J., Dewaele, S., André, L., and Muchez, P. (2013) Petrographic and mineralogical characterisation of fractionated pegmatites culminating in the Nb-Ta-Sn pegmatites of the Gatumba area (western Rwanda). Geologica Belgica, 16, 105–117.

——— (2014) Alkali metal and rare earth element evolution of rock-forming minerals from the Gatumba

722 area pegmatites (Rwanda): Quantitative assessment of crystal-melt fractionation in the regional zonation
723 of pegmatite groups. Geochimica et Cosmochimica Acta, 132, 349–374.
724 Hulsbosch, N., Boiron, M., Dewaele, S., and Muchez, P. (2016) Fluid fractionation of tungsten during
725 granite-pegmatite differentiation and the metal source of peribatholitic W quartz veins: Evidence from
726 the Karagwe-Ankole Belt (Rwanda). Geochimica et Cosmochimica Acta, 175, 299–318.
727 Husson, E., Repelin, Y., Dao, N.Q., and Brusset, H. (1977) Etude par spectrophotométries d'absorption
728 infrarouge et de diffusion Raman des niobates de structure columbite. Spectrochimica Acta Part A:
729 Molecular Spectroscopy, 33, 995-1001. (in French).
730 Kaeter, D., Barros, R., and Menuge, J.F. (2021) Metasomatic high field strength element, tin, and base metal
731 enrichment processes in lithium pegmatites from Southeast Ireland. Economic Geology, 116, 169–198.
732 Keppler, H. (1994) Partitioning of phosphorus between melt and fluid in the system haplogranite-H_2O-P_2O_5.
733 Chemical Geology, 117, 345–353.
734 Kontak, D.J. (2006) Nature and origin of an LCT-suite pegmatite with late-stage sodium enrichment, Brazil
735 Lake, Yarmouth County, Nova Scotia. I. Geological setting and petrology. The Canadian Mineralogist,
736 44, 563–598.
737 Kularatne, K., and Audétat, A. (2014) Rutile solubility in hydrous rhyolite melts at 750-900 °C and 2 kbar,
738 with application to titanium-in-quartz (TitaniQ) thermobarometry. Geochimica et Cosmochimica Acta,
739 125, 196–209.
740 Linnen, R.L. (1998) The solubility of Nb-Ta-Zr-Hf-W in granitic melts with Li and Li + F: Constraints for
741 mineralization in rare metal granites and pegmatites. Economic Geology, 93, 1013–1025.
742 Linnen, R.L., and Cuney, M. (2005) Granite-related rare-element deposits and experimental constraints on
743 Ta-Nb-W-Sn-Zr-Hf mineralization. Rare-Element Geochemistry and Mineral Deposits, 17, 45–68.
744 Linnen, R.L., and Keppler, H. (1997) Columbite solubility in granitic melts: Consequences for the
745 enrichment and fractionation of Nb and Ta in the Earth's crust. Contributions to Mineralogy and
746 Petrology, 128, 213–227.

747 Linnen, R.L., Van Lichtervelde, M., and Černý, P. (2012) Granitic pegmatites as sources of strategic metals.
748 Elements, 8, 275–280.
749 Llorens, T., García Polonio, F., López-Moro, F.J., Fernández Fernández, A., Sanz Contreras, J.L., and Moro,
750 M.C. (2017) Tin-tantalum-niobium mineralization in the Penouta deposit (NW Spain): Textural features
751 and mineral chemistry to unravel the genesis and evolution of cassiterite and columbite group minerals
752 in a peraluminous system. Ore Geology Reviews, 81, 79–95.
753 London, D. (1987) Internal differentiation of rare-element pegmatites: Effects of boron, phosphorus, and
754 fluorine. Geochimica et Cosmochimica Acta, 51, 403–420.
755 ——— (2018) Ore-forming processes within granitic pegmatites. Ore Geology Reviews, 101, 349–383.
756 London, D., and Burt, D.M. (1982) Alteration of spodumene, montebrasite and lithiophilite in pegmatites of
757 the White Picacho district, Arizona. American Mineralogist, 67, 97–113.
758 London, D., Hervig, R.L., and Morgan VI, G.B. (1988) Melt-vapor solubilities and elemental partitioning in
759 peraluminous granite-pegmatite systems: experimental results with Macusani glass at 200 MPa.
760 Contributions to Mineralogy and Petrology, 99, 360–373.
761 London, D., Morgan VI, G.B., Babb, H.A., and Loomis, J.L. (1993) Behavior and effects of phosphorus in
762 the system Na_2O-K_2O-Al_2O_3-SiO_2-P_2O_5-H_2O at 200 MPa(H_2O). Contributions to Mineralogy and
763 Petrology, 113, 450–465.
764 London, D., Wolf, M.B., Morgan VI, G.B., and Garrido, M.G. (1999) Experimental silicate-phosphate
765 equilibria in peraluminous granitic magmas, with a case study of the Alburquerque batholith at Tres
766 Arroyos, Badajoz, Spain. Journal of Petrology, 40, 215–240.
767 McNeil, A.G., Linnen, R.L., Flemming, R.L., and Fayek, M. (2020) An experimental approach to examine
768 fluid-melt interaction and mineralization in rare-metal pegmatites. American Mineralogist, 105, 1078–
769 1087.
770 Melcher, F., Graupner, T., Gäbler, H.-E., Sitnikova, M., Henjes-Kunst, F., Oberthür, T., Gerdes, A., and
771 Dewaele, S. (2015) Tantalum-(niobium-tin) mineralisation in African pegmatites and rare metal

granites: Constraints from Ta-Nb oxide mineralogy, geochemistry and U-Pb geochronology. Ore Geology Reviews, 64, 667–719.

Monteyne-Poulaert, G., Delwiche, R., and Cahen, L. (1963) Ages de minéralisations pegmatitiques et filoniennes du Rwanda et du Burundi. Bullletin de la Société Belge de Géologie, de Paléontologie et d'Hydrologie, LIII, 1-13. (in French).

Moore, P.B. (1973) Pegmatite phosphates: descriptive mineralogy and crystal chemistry. Mineralogical Record, 4, 103–130.

Moreira, R.L., Rubinger, C.P.L., Krambrock, K., and Dias, A. (2010) Polarized Raman scattering and infrared spectroscopy of a natural manganocolumbite single crystal. Journal of Raman Spectroscopy, 41, 1044–1049.

Muchez, P., Hulsbosch, N., and Dewaele, S. (2014) Geological mapping and implications for Nb-Ta, Sn and W prospection in Rwanda. Mededelingen Zittingen Koninklijke Academie Overzeese Wetenschappen, 60, 515–530.

Nambaje, C., Williams, I.S., and Sajeev, K. (2021) SHRIMP U-Pb dating of cassiterite: Insights into the timing of Rwandan tin mineralisation and associated tectonic processes. Ore Geology Reviews, 135, 104185.

Pohl, W.L., Biryabarema, M., and Lehmann, B. (2013) Early Neoproterozoic rare metal (Sn, Ta, W) and gold metallogeny of the Central Africa Region: a review. Applied Earth Science, 122, 66–82.

Polinard, E. (1950) La montebrasite de Buranga. In Troisiè e Congrès National des Sciences (Bruxelles) Vol. I, pp. 18-19. (in French). Brussels.

Porto, S.P.S., Fleury, P.A., and Damen, T.C. (1967) Raman spectra of TiO_2, MgF_2, ZnF_2, FeF_2, and MnF_2. Physical Review, 154, 522–526.

Raimbault, L., Cuney, M., Azencott, C., Duthou, J.L., and Joron, J.L. (1995) Geochemical evidence for a multistage magmatic genesis of Ta-Sn-Li mineralization in the granite at Beauvoir, French Massif Central. Economic Geology, 90, 548–576.

797 Roda-Robles, E., Vieira, R., Pesquera, A., and Lima, A. (2010) Chemical variations and significance of
798 phosphates from the Fregeneda-Almendra pegmatite field, Central Iberian Zone (Spain and Portugal).
799 Mineralogy and Petrology, 100, 23–34.
800 Roda-Robles, E., Galliski, M.Á., Roquet, B., Hatert, F., and de Parseval, P. (2012) Phosphate nodules
801 containing two distinct assemblages in the Cema granitic pegmatite, San Luis province, Argentina:
802 Paragenesis, composition and significance. The Canadian Mineralogist, 50, 913–931.
803 Roda-Robles, E., Pesquera, A., Simmons, W., Gil-Crespo, P.P., Webber, K.L., Nizamoff, J., and Falster, A.
804 (2020) Paragenetic relationships, geochemistry and petrogenetic significance of primary Fe-Mn
805 phosphates from pegmatites: The case study of Cañada (Salamanca, Spain) and Palermo (New
806 Hampshire, USA) pegmatites. Lithos, 374–375, 105710.
807 Roda, E., Pesquera, A., Fontan, F., and Keller, P. (2004) Phosphate mineral association in the Cañada
808 pegmatite (Salamanca, Spain): Paragenetic relationships, chemical compositions, and implications for
809 pegmatite evolution. American Mineralogist, 89, 110–125.
810 Ryerson, F.J., and Watson, E.B. (1987) Rutile saturation in magmas: implications for Ti-Nb-Ta depletion in
811 island-arc basalts. Earth and Planetary Science Letters, 86, 225–239.
812 Schmid-Beurmann, P., Knitter, S., and Cemič, L. (2000) P-T stability of the lazulite-scorzalite solid-solution
813 series. Mineralogy and Petrology, 70, 55–71.
814 Siachoque, A., Garcia, R., and Vlach, S.R.F. (2020) Occurrence and composition of columbite-(Fe) in the
815 reduced A-type Desemborque pluton, Graciosa Province (S-SE Brazil). Minerals, 10, 411.
816 Simmons, W.B., and Webber, K.L. (2008) Pegmatite genesis: state of the art. European Journal of
817 Mineralogy, 20, 421–438.
818 Stepanov, A., Mavrogenes, J.A., Meffre, S., and Davidson, P. (2014) The key role of mica during igneous
819 concentration of tantalum. Contributions to Mineralogy and Petrology, 167, 1–8.
820 Tack, L., Wingate, M.T.D., De Waele, B., Meert, J.G., Belousova, E.A., Griffin, B., Tahon, A., and
821 Fernandez-Alonso, M. (2010) The 1375 Ma “Kibaran event” in Central Africa: Prominent emplacement

of bimodal magmatism under extensional regime. Precambrian Research, 180, 63–84.

Tang, Y., and Zhang, H. (2015) An experimental determination of W, Nb, and Ta partition coefficients between P-rich peraluminous granitic melt and coexisting aqueous fluid. Chinese Journal of Geochemistry, 34, 194–200.

Timofeev, A., and Williams-Jones, A.E. (2015) The origin of niobium and tantalum mineralization in the Nechalacho REE deposit, NWT, Canada. Economic Geology, 110, 1719–1735.

Timofeev, A., Migdisov, A.A., and Williams-Jones, A.E. (2015) An experimental study of the solubility and speciation of niobium in fluoride-bearing aqueous solutions at elevated temperature. Geochimica et Cosmochimica Acta, 158, 103–111.

Van Daele, J., Hulsbosch, N., Dewaele, S., and Muchez, P. (2020) Metamorphic and metasomatic evolution of the Western Domain of the Karagwe-Ankole Belt (Central Africa). Journal of African Earth Sciences, 165, 103783.

Van Lichtervelde, M., Salvi, S., Beziat, D., and Linnen, R.L. (2007) Textural features and chemical evolution in tantalum oxides: Magmatic versus hydrothermal origins for Ta mineralization in the Tanco Lower pegmatite, Manitoba, Canada. Economic Geology, 102, 257–276.

Van Lichtervelde, M., Holtz, F., and Melcher, F. (2018) The effect of disequilibrium crystallization on Nb-Ta fractionation in pegmatites: Constraints from crystallization experiments of tantalite-tapiolite. American Mineralogist, 103, 1401–1416.

Varlamoff, N. (1961) Matériaux pour l'étude des pegmatites du Congo et du Ruanda. IV. Pegmatites à amblygonite et à spodumène et pegmatites fortement albitisées à spodumène et à cassitérite de la région de Katumba (Ruanda). Annales de la Société Géologique de Belgique, 84, 257-278. (in French).

——— (1963) Les phénomène de greisenification, d'albitisation et de lepidolitisation et leurs relations spatiales avec les granites et les pegmatites granitiques d'Afrique. Bulletin-Société géologique de Belgique, 5, 285-322. (in French).

——— (1972) Central and West African rare-metal granitic pegmatites, related aplites, quartz veins and

847 mineral deposits. Mineralium Deposita, 7, 202–216.

848 Webster, J.D., Thomas, R., Rhede, D., Förster, H.J., and Seltmann, R. (1997) Melt inclusions in quartz from
849 an evolved peraluminous pegmatite: Geochemical evidence for strong tin enrichment in fluorine-rich
850 and phosphorus-rich residual liquids. Geochimica et Cosmochimica Acta, 61, 2589–2604.

851 Wise, M.A., Francis, C.A., and Černý, P. (2012) Compositional and structural variations in columbite-group
852 minerals from granitic pegmatites of the Brunswick and Oxford fields, Maine: Differential trends in F-
853 poor and F-rich environments. Canadian Mineralogist, 50, 1515–1530.

854 Zajacz, Z., Halter, W.E., Pettke, T., and Guillong, M. (2008) Determination of fluid/melt partition
855 coefficients by LA-ICPMS analysis of co-existing fluid and silicate melt inclusions: Controls on
856 element partitioning. Geochimica et Cosmochimica Acta, 72, 2169–2197.

857 Zaraisky, G.P., Korzhinskaya, V., and Kotova, N. (2010) Experimental studies of Ta_2O_5 and columbite-
858 tantalite solubility in fluoride solutions from 300 to 550°C and 50 to 100 MPa. Mineralogy and
859 Petrology, 99, 287–300.

860

861

862

This is the peer-reviewed, final accepted version for American Mineralogist, published by the Mineralogical Society of America.
The published version is subject to change. Cite as Authors (Year) Title. American Mineralogist, in press.
DOI: https://doi.org/10.2138/am-2022-8201. http://www.minsocam.org/

Table 1: representative WDS analyses of NTO from each facies from the Buranga dike. Oxide mass% values and recalculated atomic proportions are provided. Analyses were recalculated on the basis of 24 oxygens. SAPN = strongly altered phosphatic nodules. PAPN = partially altered phosphatic nodules.

Facies	Phosphatic nodules																Albitized			
Group	PAPN					SAPN		PAPN					SAPN							
mineral	rutile core	rutile core	rutile rim	rutile rim	rutile patchy	rutile core	rutile rim	CGM core	CGM core	CGM rim	CGM rim	CGM patchy	CGM core	CGM rim	CGM patchy	CGM patchy	CGM core	CGM core	CGM rim	CGM rim
Mass%																				
Nb_2O_5	6.1	10.6	6.4	8.5	7.6	12.9	11.3	43.9	36.1	37.7	48.2	51.1	60.1	51.4	58.9	71.0	70.4	64.3	62.4	48.4
Ta_2O_5	1.7	5.3	11.1	4.0	10.1	10.6	16.9	35.9	42.1	41.8	31.3	28.8	17.9	29.2	21.7	7.4	8.9	16.1	18.3	33.7
TiO_2	89.6	78.6	77.3	81.7	76.8	67.5	61.1	1.9	3.2	2.3	2.0	1.6	2.0	1.3	0.7	0.9	0.5	0.5	0.3	0.6
SnO_2	1.3	1.3	0.8	1.2	0.6	1.9	1.8	0.6	0.9	0.9	0.5	0.4	0.5	0.5	0.2	0.1	0.1	0.1	0.0	0.1
FeO	2.6	4.2	4.8	4.4	5.4	6.5	7.6	9.9	10.2	9.9	10.1	9.6	9.8	9.9	8.6	8.5	14.8	12.2	12.7	13.1
MnO	0.0	0.0	0.0	0.0	0.0	0.0	0.1	6.0	5.0	5.4	6.5	7.1	7.6	6.6	8.7	9.7	3.7	5.7	4.9	3.2
Total	101.4	100.4	100.6	100.3	100.6	99.9	99.2	98.2	97.4	98	98.5	98.6	97.9	99	98.8	98.2	98.4	98.9	98.6	99
a.p.f.u																				
Nb	0.45	0.83	0.51	0.66	0.61	1.07	0.99	5.25	4.47	4.64	5.62	5.89	6.64	5.92	6.58	7.47	7.49	7.01	6.89	5.69
Ta	0.08	0.25	0.53	0.19	0.48	0.53	0.88	2.59	3.14	3.09	2.19	2.00	1.19	2.02	1.46	0.47	0.57	1.06	1.22	2.39
Ti	11.05	10.21	10.26	10.48	10.17	9.30	8.85	0.38	0.65	0.48	0.39	0.30	0.37	0.25	0.13	0.15	0.1	0.09	0.05	0.11
Sn	0.08	0.09	0.06	0.08	0.04	0.14	0.14	0.07	0.09	0.10	0.05	0.04	0.05	0.05	0.02	0.01	0.01	0.01	0.00	0.01
Fe	0.36	0.61	0.7	0.62	0.79	1.00	1.22	2.19	2.32	2.26	2.18	2.05	2.00	2.11	1.78	1.65	2.91	2.46	2.59	2.86
Mn	0.00	0.00	0.00	0.00	0.00	0.00	0.01	1.33	1.16	1.24	1.41	1.53	1.57	1.42	1.81	1.92	0.73	1.17	1.01	0.7
Sum	12.06	12.05	12.1	12.12	12.13	12.12	12.17	11.8	11.85	11.81	11.85	11.82	11.82	11.78	11.79	11.86	11.81	11.8	11.78	11.76

866

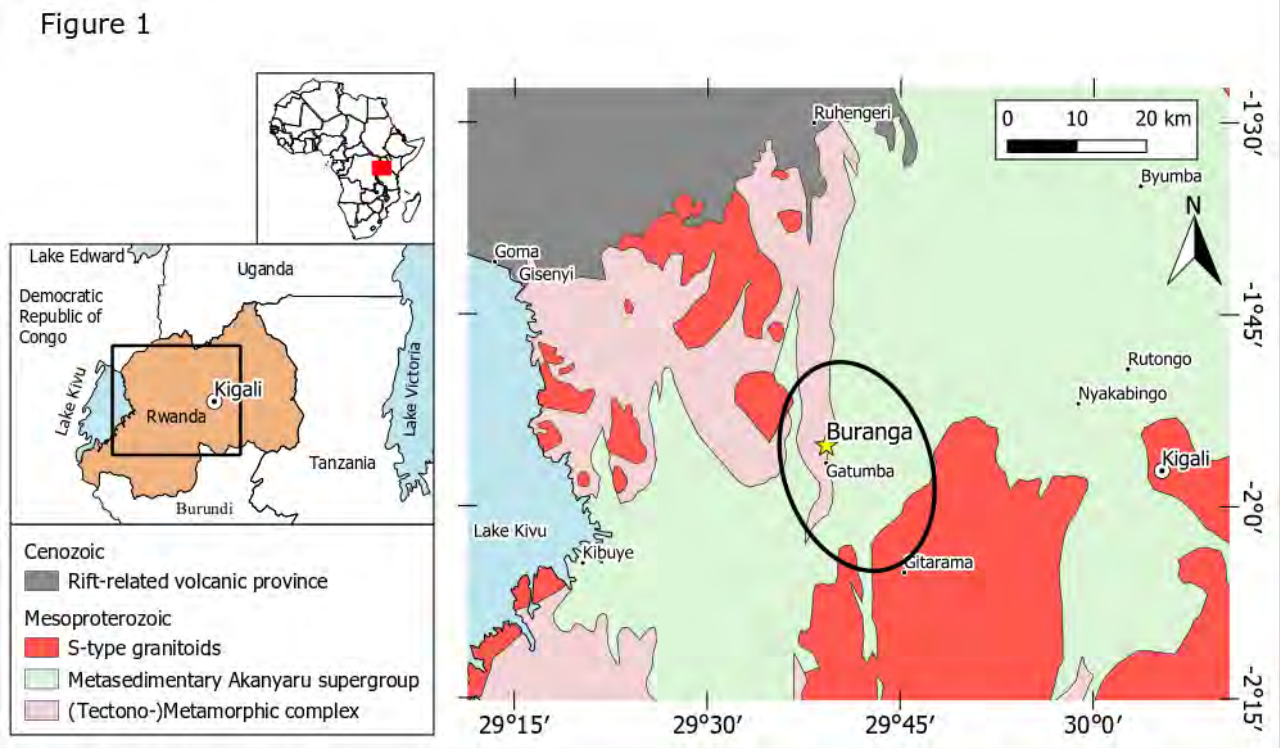

867

868 **Figure 1:** Simplified geological map of western Rwanda, with the location of the Gatumba pegmatite field (ellipsoid) and the Buranga
869 pegmatite (star). Modified from Fernandez-Alonso et al. (2007).

This is the peer-reviewed, final accepted version for American Mineralogist, published by the Mineralogical Society of America.
The published version is subject to change. Cite as Authors (Year) Title. American Mineralogist, in press.
DOI: https://doi.org/10.2138/am-2022-8201. http://www.minsocam.org/

Figure 2

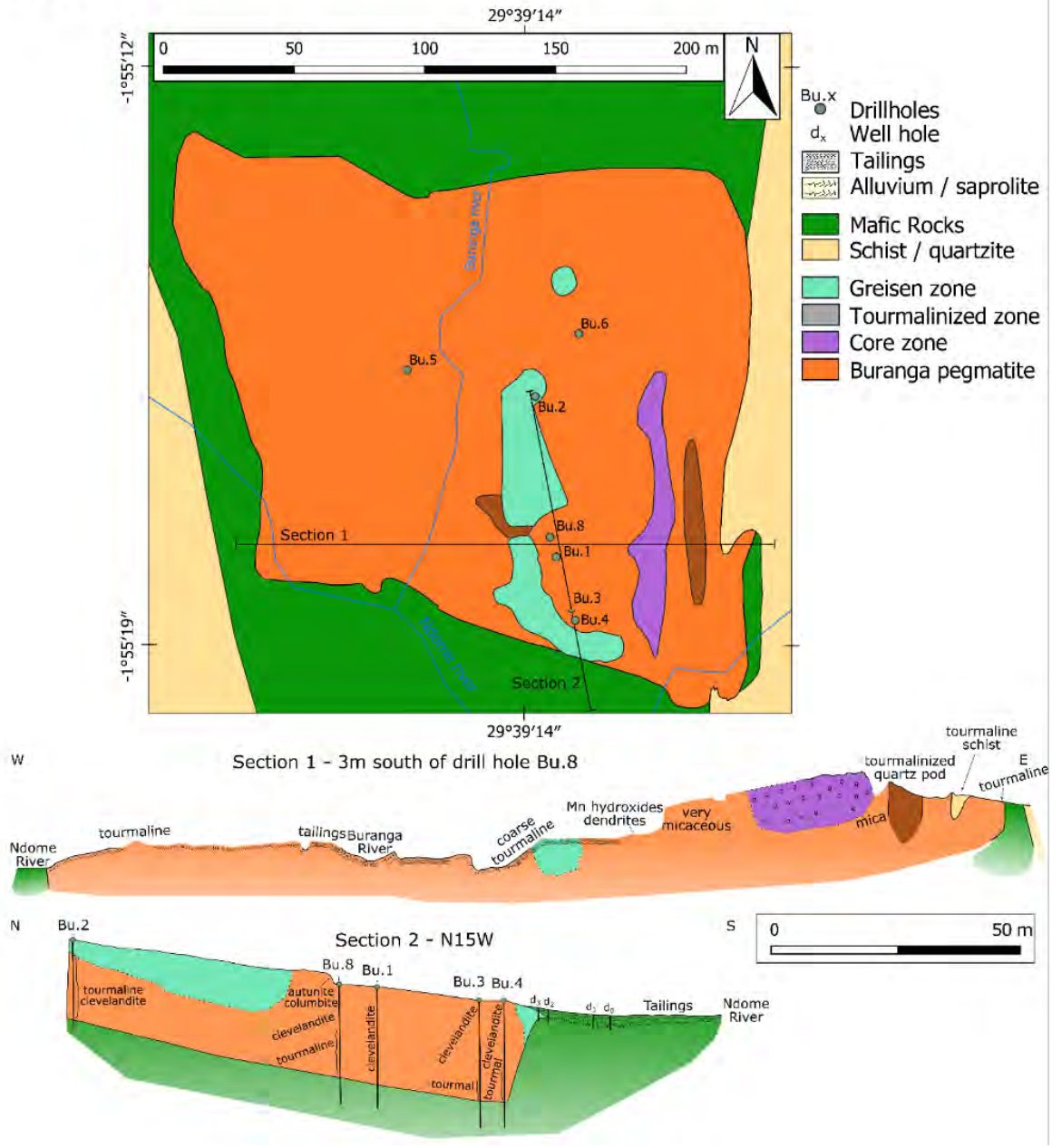

Figure 2: Local geological map of the Buranga pegmatite and cross-sections through the dike. Digitalized from exploration reports of the Minetain company (1955-1956) present in the archives of the Royal Museum for Central Africa (Belgium).

This is the peer-reviewed, final accepted version for American Mineralogist, published by the Mineralogical Society of America.
The published version is subject to change. Cite as Authors (Year) Title. American Mineralogist, in press.
DOI: https://doi.org/10.2138/am-2022-8201. http://www.minsocam.org/

Figure 3

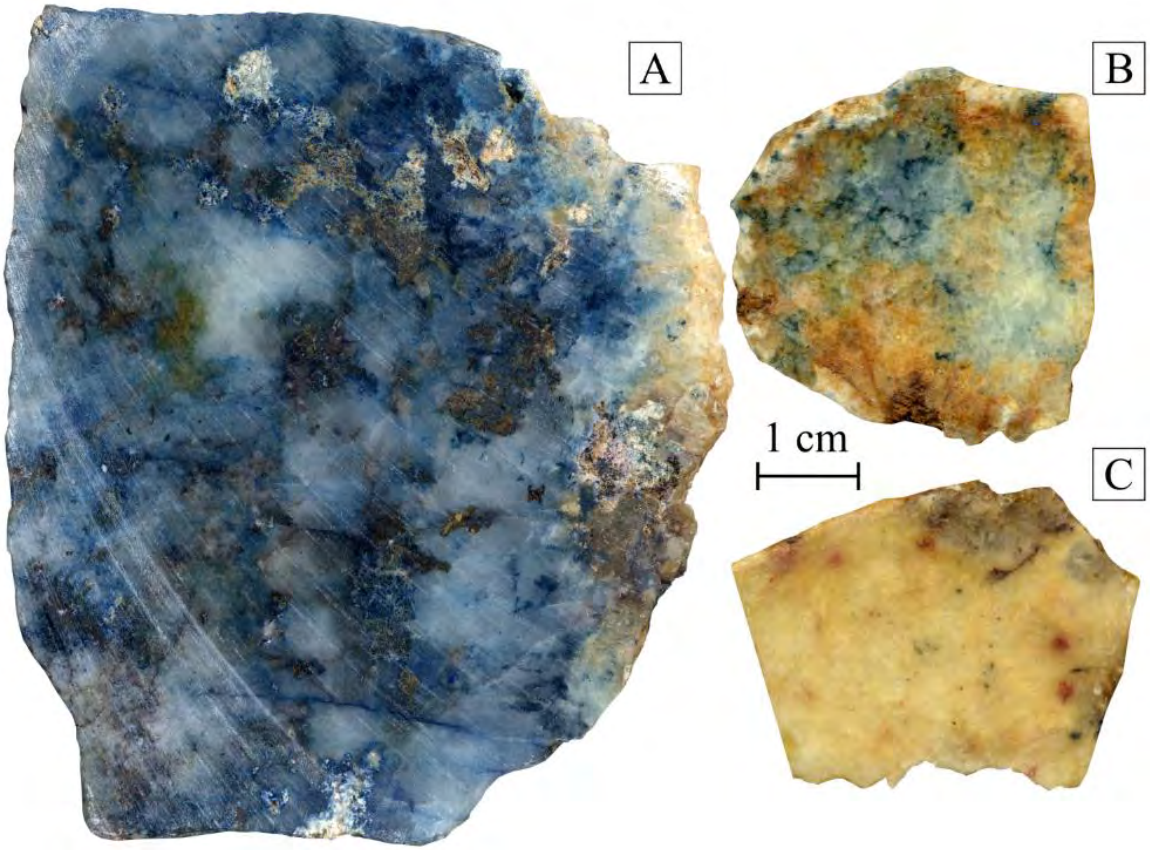

873

874 **Figure 3:** Hand samples from the Buranga pegmatite examined in this study. **(a)** Sample BU19 (RGM9705, in the notation of the Royal
875 Museum for Central Africa), partially altered phosphatic nodule dominated by trolleite (light blue) with altered crystals of rosemaryite (brownish)
876 and scattered scorzalite (dark blue). The right part of the sample is composed of secondary brazilianite (cream-colored to white). The concentric
877 diagonal curves, especially visible at the bottom left of the sample, are saw scratches. **(b)** Sample BU04 (RGM9696), strongly altered phosphatic
878 nodule composed of bertossaite (pinkish cream), trolleite (light blue), brazilianite (white cream), and scorzalite (dark blue spots). **(c)** Sample
879 BU24 (RGM8894), albitized facies, composed mainly of albite (cream-colored) with oxidation spots (reddish spots) and few tourmaline crystals
880 (black spots).

881

882

883

884

This is the peer-reviewed, final accepted version for American Mineralogist, published by the Mineralogical Society of America.
The published version is subject to change. Cite as Authors (Year) Title. American Mineralogist, in press.
DOI: https://doi.org/10.2138/am-2022-8201. http://www.minsocam.org/

Figure 4

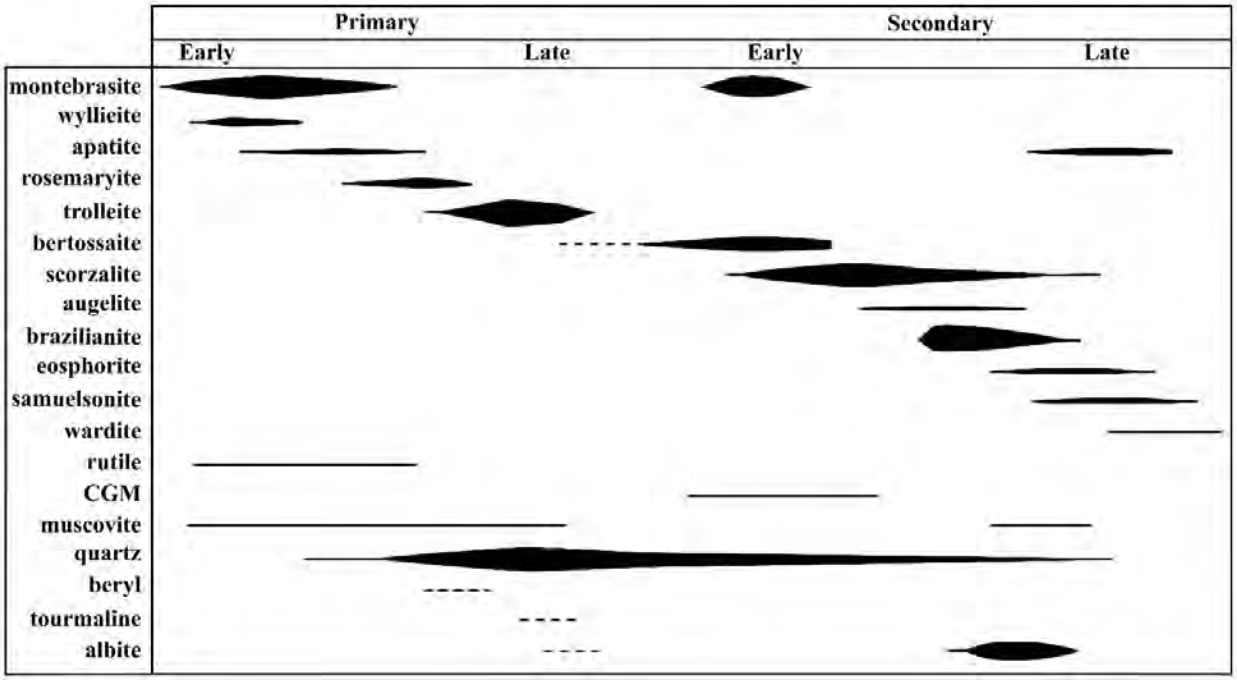

Figure 4: Paragenesis for the phosphatic nodules and albitized facies from the Buranga pegmatite. The thickness of the lines is an indication of the mineral's relative abundance (i.e., the thicker the line, the more abundant the mineral is). Dashed lines are uncertain positioning, mostly due to a lack of unequivocal textural relations with other minerals or multiple textural contexts.

This is the peer-reviewed, final accepted version for American Mineralogist, published by the Mineralogical Society of America.
The published version is subject to change. Cite as Authors (Year) Title. American Mineralogist, in press.
DOI: https://doi.org/10.2138/am-2022-8201. http://www.minsocam.org/

Figure 5

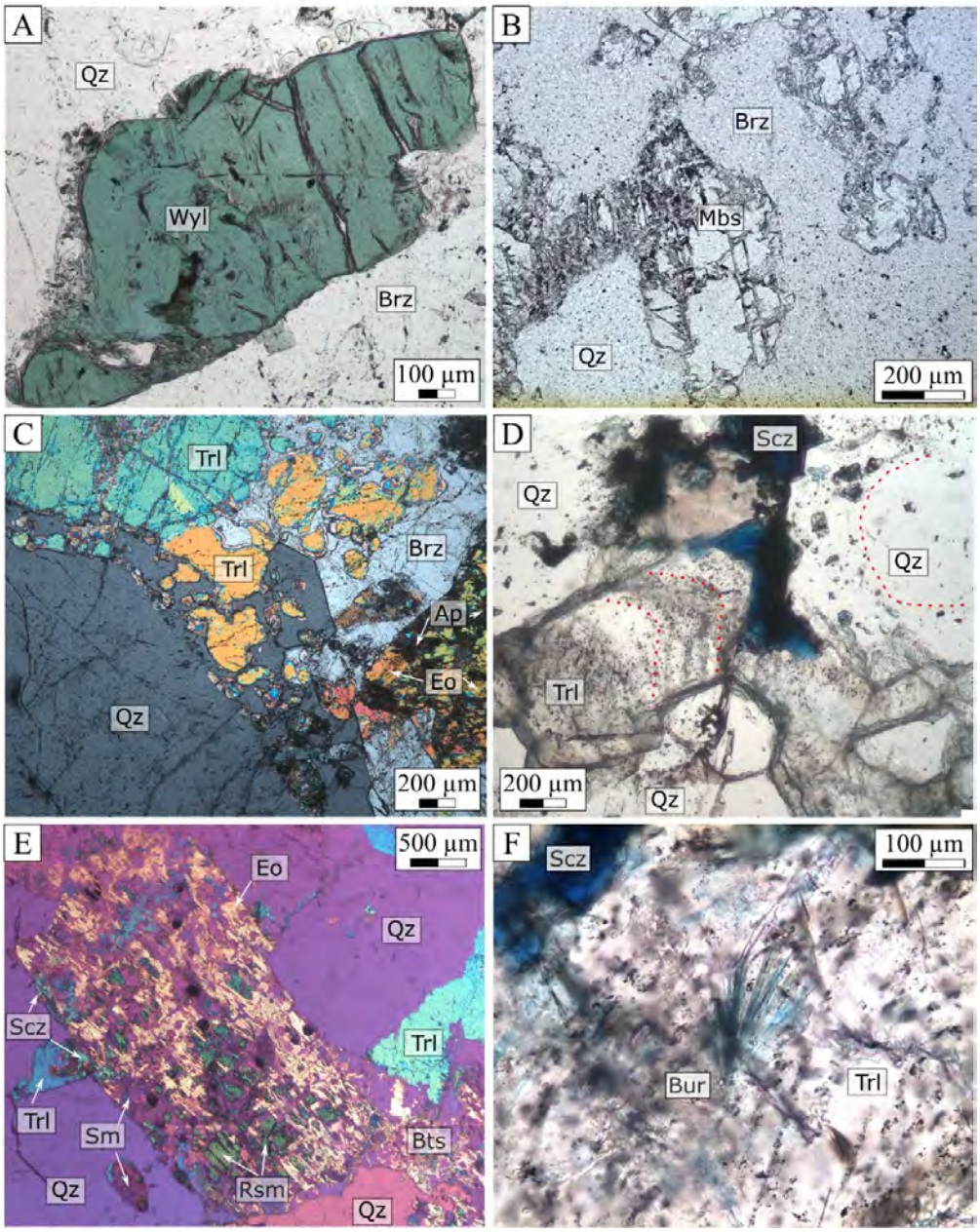

Figure 5: Optical photomicrographs from the Al-rich phosphatic nodules from the Buranga pegmatite. **(a)** Anhedral wyllieite crystal surrounded by brazilianite and quartz. Plane polarizers. **(b)** Anhedral and fractured montebrasite crystal surrounded by coarse-grained brazilianite and quartz. Plane polarizers. **(c)** Partially resorbed trolleite crystal enclosed by euhedral quartz and brazilianite. Crossed polarizers. **(d)** Subhedral trolleite surrounded by interstitial scorzalite and euhedral quartz. Note primary fluid inclusions aligned in growth zones of trolleite, and the mixture of fluid, melt, and crystal inclusions in the quartz grain on the top right (dotted lines). Plane polarizers. **(e)** Pseudomorph after rosemaryite partially replaced by a combination of eosphorite, and samuelsonite. Bertossaite partially rims the bottom part of the pseudomorph. Scorzalite grows in the contacts with trolleite. Gypsum plate inserted. **(f)** Euhedral radiating crystals of burangaite replacing trolleite. Plane polarizers.

Mineral abbreviations: Brz = brazilianite; Bts = bertossaite; Bur = burangaite; Eo = eosphorite; Mbs = montebrasite; Qz = quartz; Rsm = rosemaryite; Scz = scorzalite; Sm = samuelsonite; Trl = trolleite; Wyl = wyllieite.

This is the peer-reviewed, final accepted version for American Mineralogist, published by the Mineralogical Society of America.
The published version is subject to change. Cite as Authors (Year) Title. American Mineralogist, in press.
DOI: https://doi.org/10.2138/am-2022-8201. http://www.minsocam.org/

Figure 6

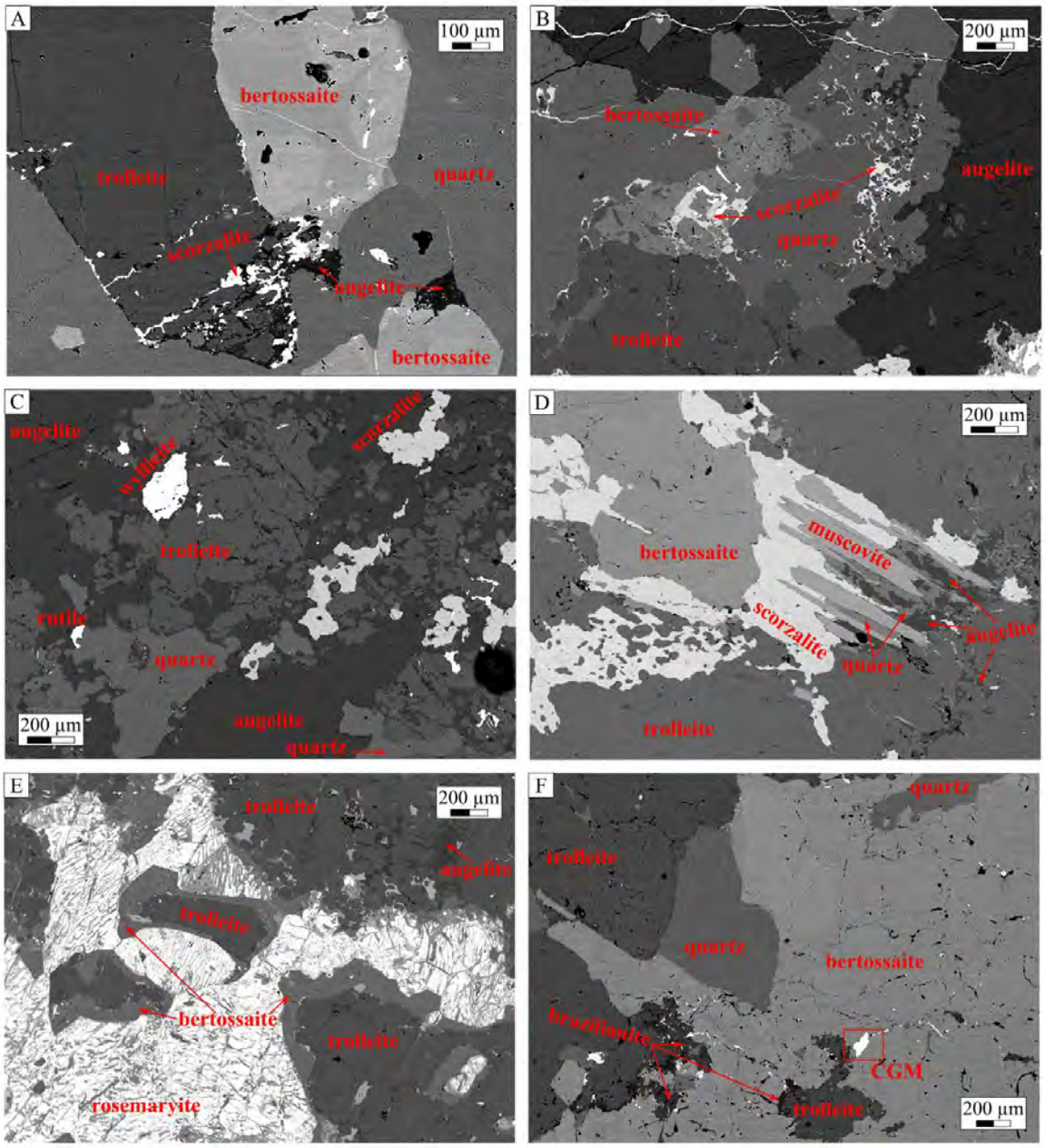

Figure 6: BSE images from the Al-rich partially (PAPN) and strongly altered phosphatic nodules (SAPN) of the Buranga pegmatite. **(a)** Subhedral trolleite in association with anhedral bertossaite, and being partially replaced by scorzalite and augelite. PAPN. **(b)** Anhedral coarse-grained trolleite surrounded by bertossaite, augelite, and quartz, with scorzalite partially replacing the finer crystals. PAPN. **(c)** Association of primary wyllieite and trolleite, partially replaced by augelite and scorzalite. Note the unaltered rutile crystal. PAPN. **(d)** Muscovite crystal partially replaced by scorzalite when in the contact with bertossaite or quartz+augelite with trolleite. SAPN. **(e)** Coarse-grained trolleite crystal developing bertossaite bands in the contacts with intensively fractured rosemaryite. PAPN. **(f)** Coarse-grained bertossaite surrounding trolleite crystal a partially altered by brazilianite. Note the CGM around the altered trolleite. This crystal is presented in detail in Fig. 6d. SAPN.

This is the peer-reviewed, final accepted version for American Mineralogist, published by the Mineralogical Society of America.
The published version is subject to change. Cite as Authors (Year) Title. American Mineralogist, in press.
DOI: https://doi.org/10.2138/am-2022-8201. http://www.minsocam.org/

Figure 7

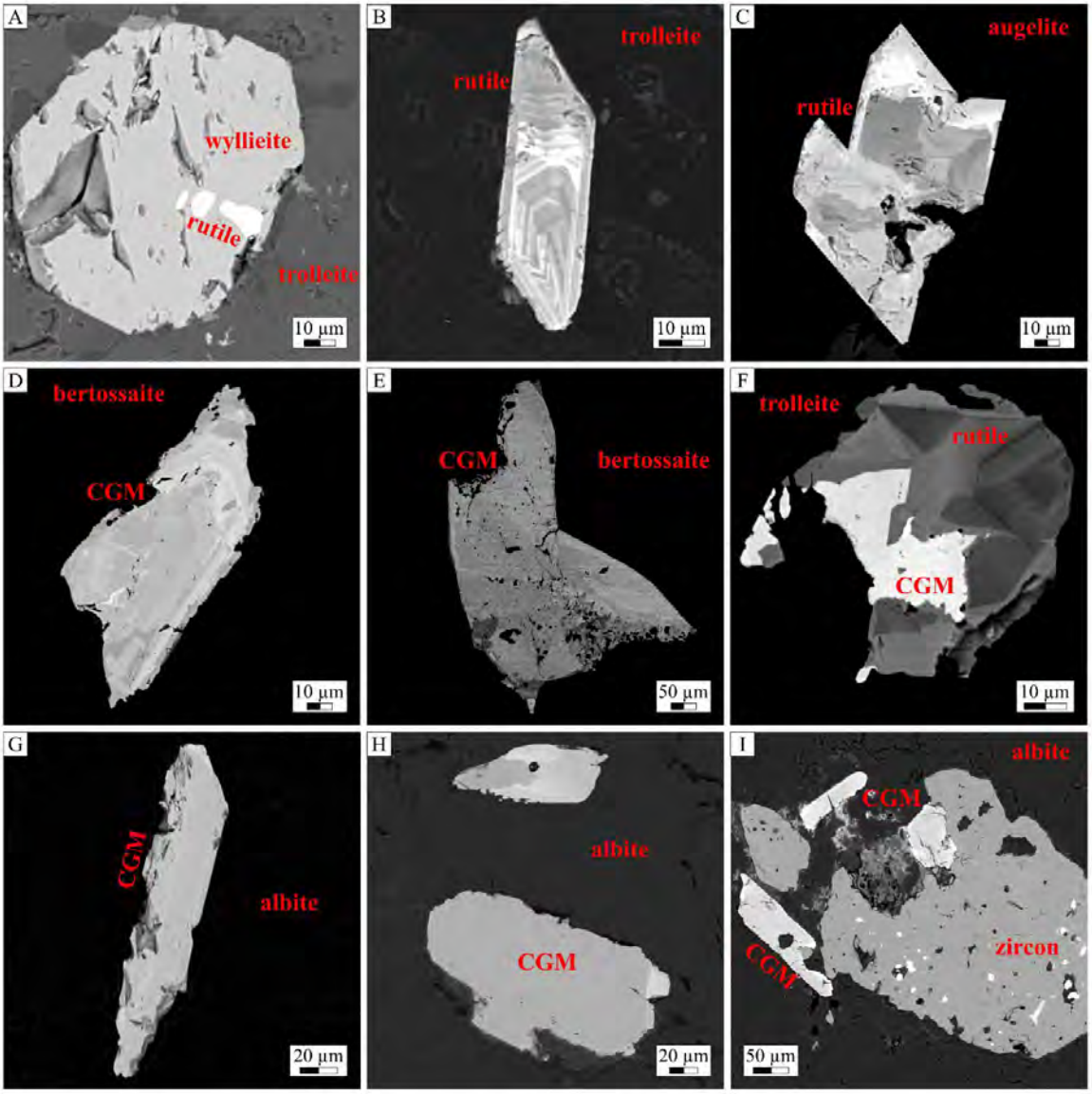

910

911 **Figure 7:** BSE images of Nb-Ta-oxide minerals from Buranga. **(a)** to **(c)** are examples of rutile from the phosphatic nodules. **(d)** and **(e)** are
912 examples of columbite-group minerals (CGM) from the phosphatic nodules. **(f)** shows a zoned rutile crystal associated with CGM. **(g)** to **(i)** are
913 CGM from the albitized facies.

914

915

This is the peer-reviewed, final accepted version for American Mineralogist, published by the Mineralogical Society of America.
The published version is subject to change. Cite as Authors (Year) Title. American Mineralogist, in press.
DOI: https://doi.org/10.2138/am-2022-8201. http://www.minsocam.org/

Figure 8

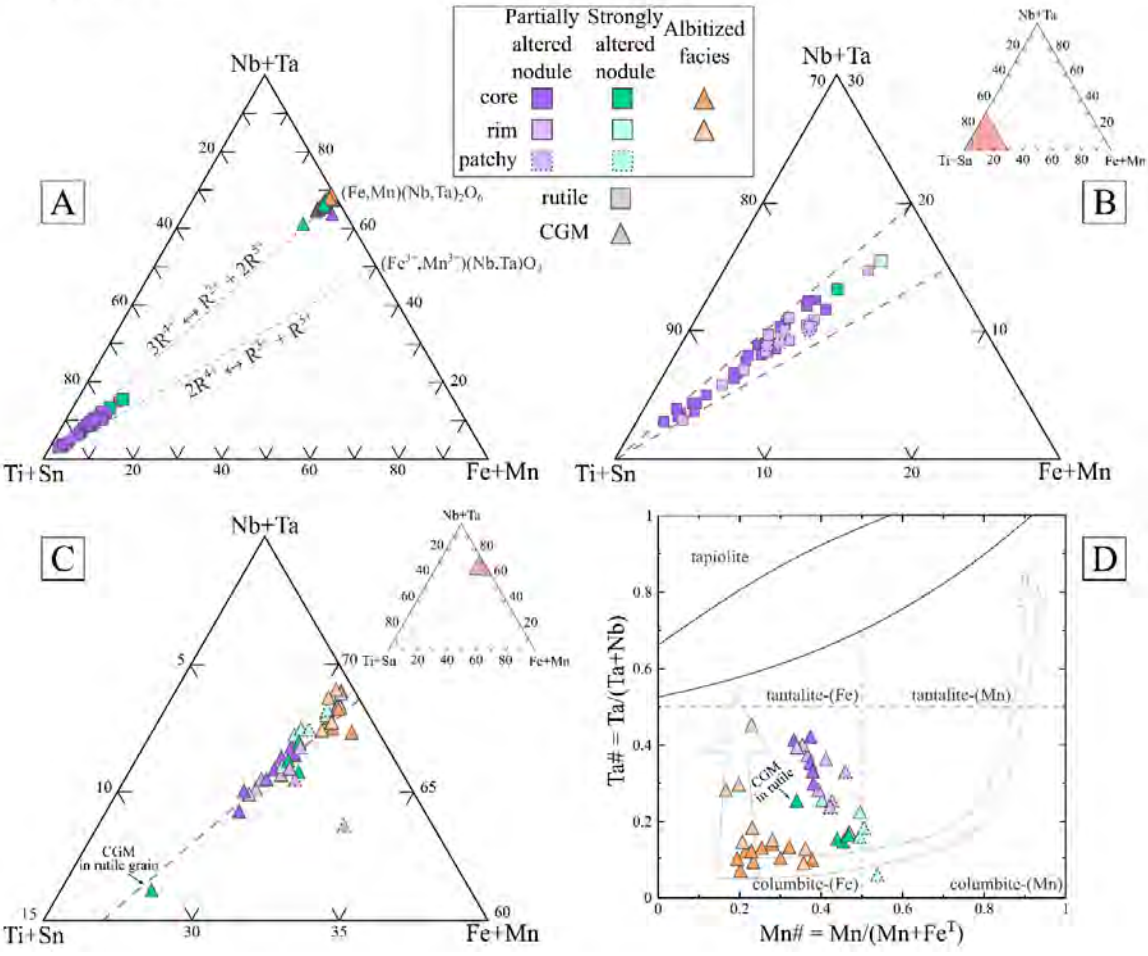

Figure 8: Cation amounts (apfu) plots from WDS analyses of Nb-Ta-oxide minerals from Buranga. **(a)** (Nb+Ta)-(Ti+Sn)-(Fe+Mn) ternary diagram for all analyses, with details for the rutile **(b)** and CGM analyses **(c)**. Ionic exchange tie-lines after Galliski et al. (2019). **(D)** CGM analyses in the quadrilateral diagram. Miscibility gap, black solid line between the tantalite and tapiolite fields, from Van Lichtervelde et al. (2018). Typical CGM fractionation trends, marked by the light grey arrows, after Černý et al. (2004) and Beurlen et al. (2008).

This is the peer-reviewed, final accepted version for American Mineralogist, published by the Mineralogical Society of America.
The published version is subject to change. Cite as Authors (Year) Title. American Mineralogist, in press.
DOI: https://doi.org/10.2138/am-2022-8201. http://www.minsocam.org/

Figure 9

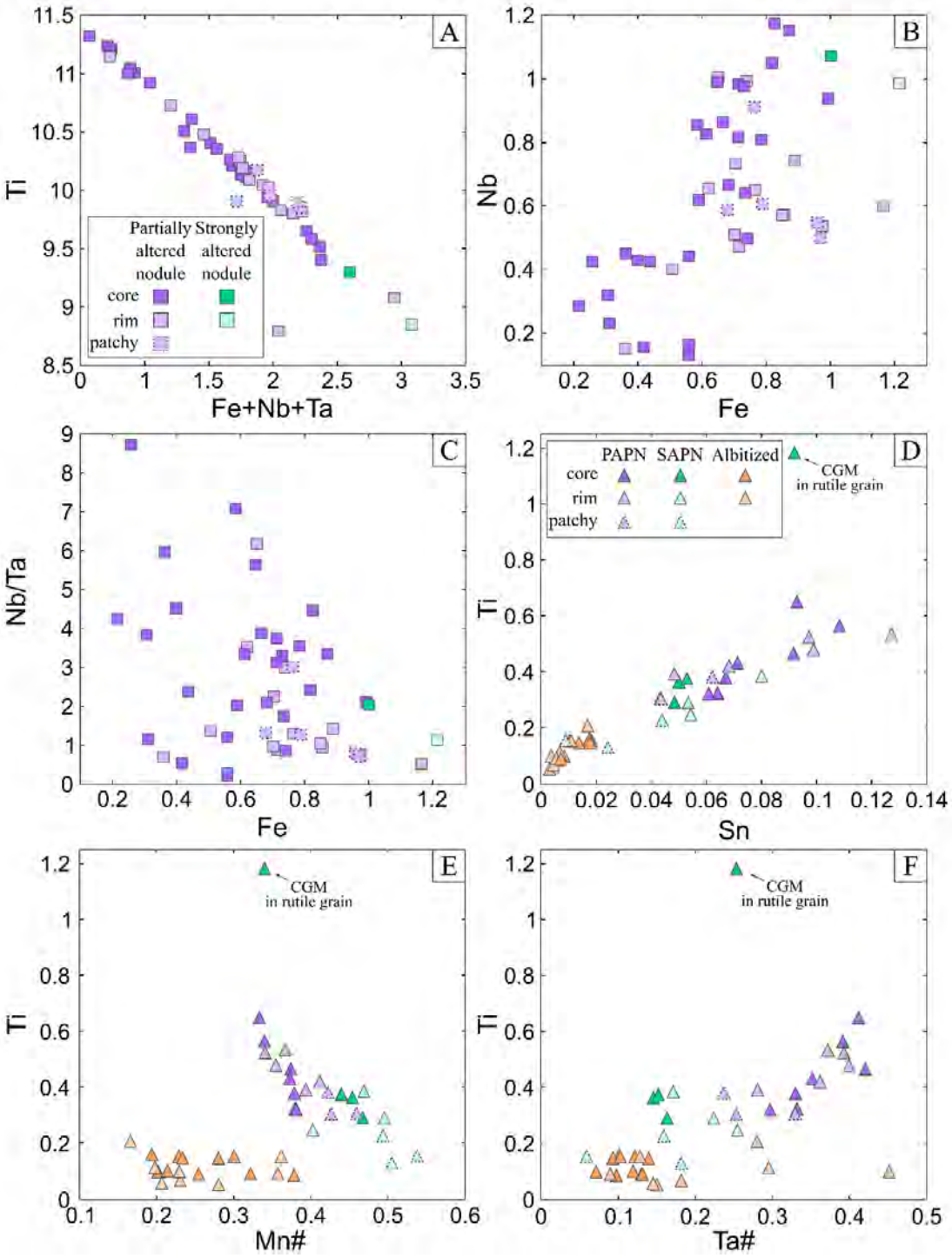

Figure 9: Cation amounts in apfu for rutile **(a, b, and c)** and CGM **(d, e, and f)** analyses from the Buranga pegmatite. Atomic ratios are defined as: Mn# = Mn/(Mn + Fe^T), and Ta# = Ta/(Ta + Nb).

This is the peer-reviewed, final accepted version for American Mineralogist, published by the Mineralogical Society of America.
The published version is subject to change. Cite as Authors (Year) Title. American Mineralogist, in press.
DOI: https://doi.org/10.2138/am-2022-8201. http://www.minsocam.org/

Figure 10

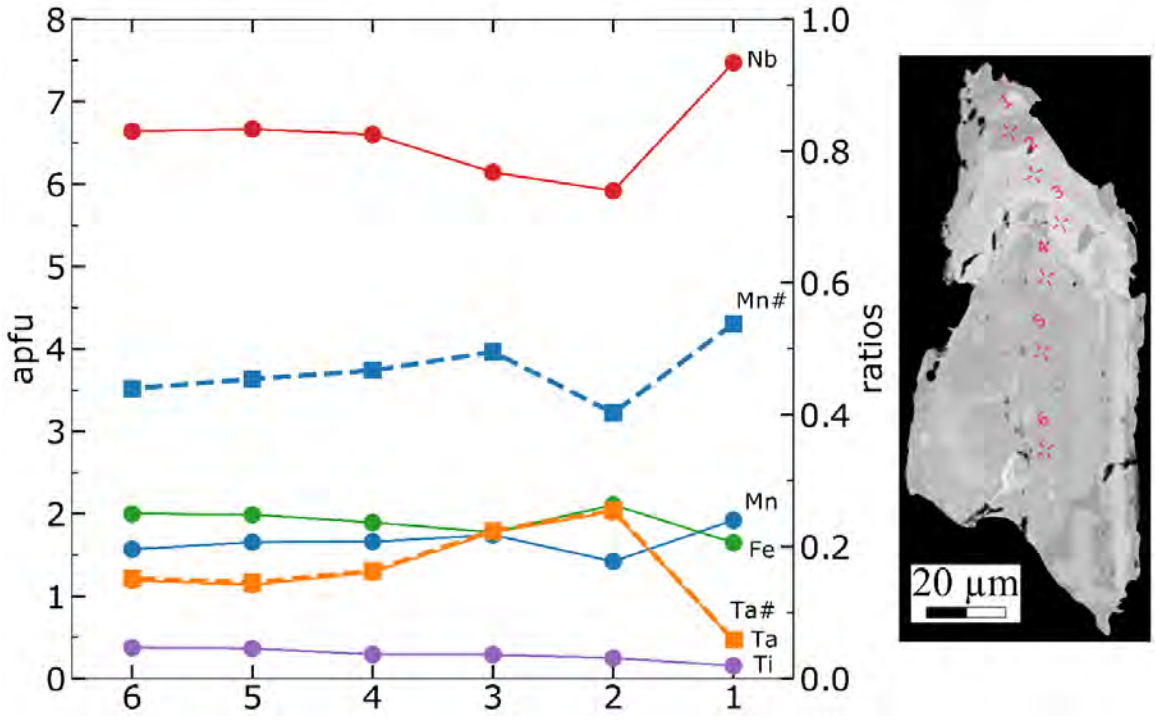

Figure 10: Chemical profile across an oscillatory zoned CGM crystal in a strongly altered phosphatic nodule from the Buranga pegmatite. Elemental values (solid lines) are reported in apfu on the left axis, while the Ta# and Mn# atomic ratios (dashed lines) are reported on the right axis.

This is the peer-reviewed, final accepted version for American Mineralogist, published by the Mineralogical Society of America.
The published version is subject to change. Cite as Authors (Year) Title. American Mineralogist, in press.
DOI: https://doi.org/10.2138/am-2022-8201. http://www.minsocam.org/

Figure 11

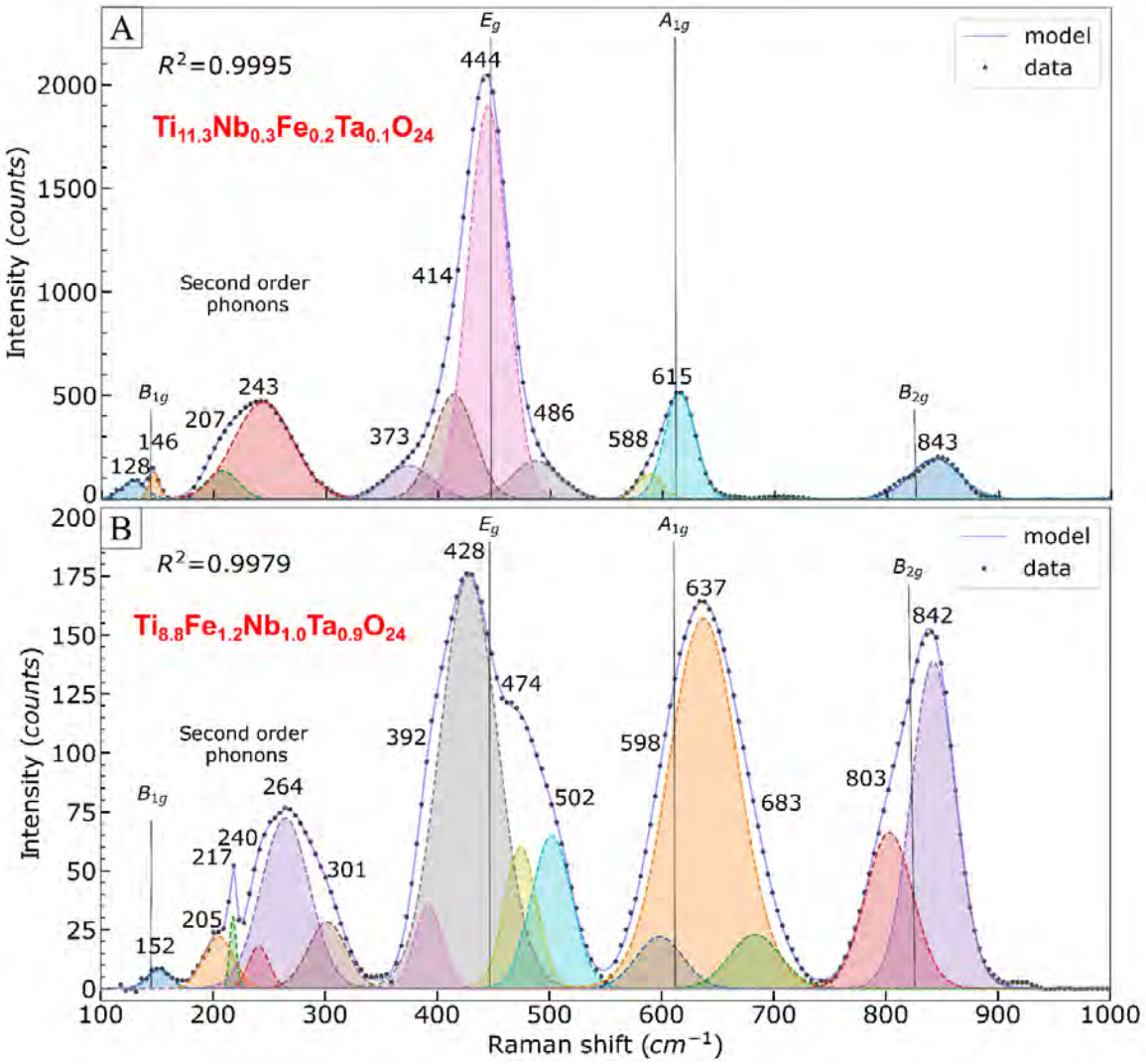

Figure 11: Raman spectra of rutile crystals from the Buranga pegmatite. **(a)** Crystal core with low Fe-Nb-Ta content from the partially altered phosphatic nodules (BU19w-ore2a). Spectrum acquired with a 532 nm laser, 150 g/mm grating, 10 % laser power, 50x long working distance objective, 30 µm confocal pinhole, two accumulations of 30 s each. **(b)** Crystal with high Fe-Nb-Ta content from the strongly altered phosphatic nodules (BU04-ore2). Analyses were carried out in the crystal core depicted in Fig. 6f. Spectrum acquired with a 532 nm laser, 150 g/mm grating, 10 % laser power, 50x long working distance objective, 30 µm confocal pinhole, two accumulations of 40 s each.

This is the peer-reviewed, final accepted version for American Mineralogist, published by the Mineralogical Society of America.
The published version is subject to change. Cite as Authors (Year) Title. American Mineralogist, in press.
DOI: https://doi.org/10.2138/am-2022-8201. http://www.minsocam.org/

Figure 12

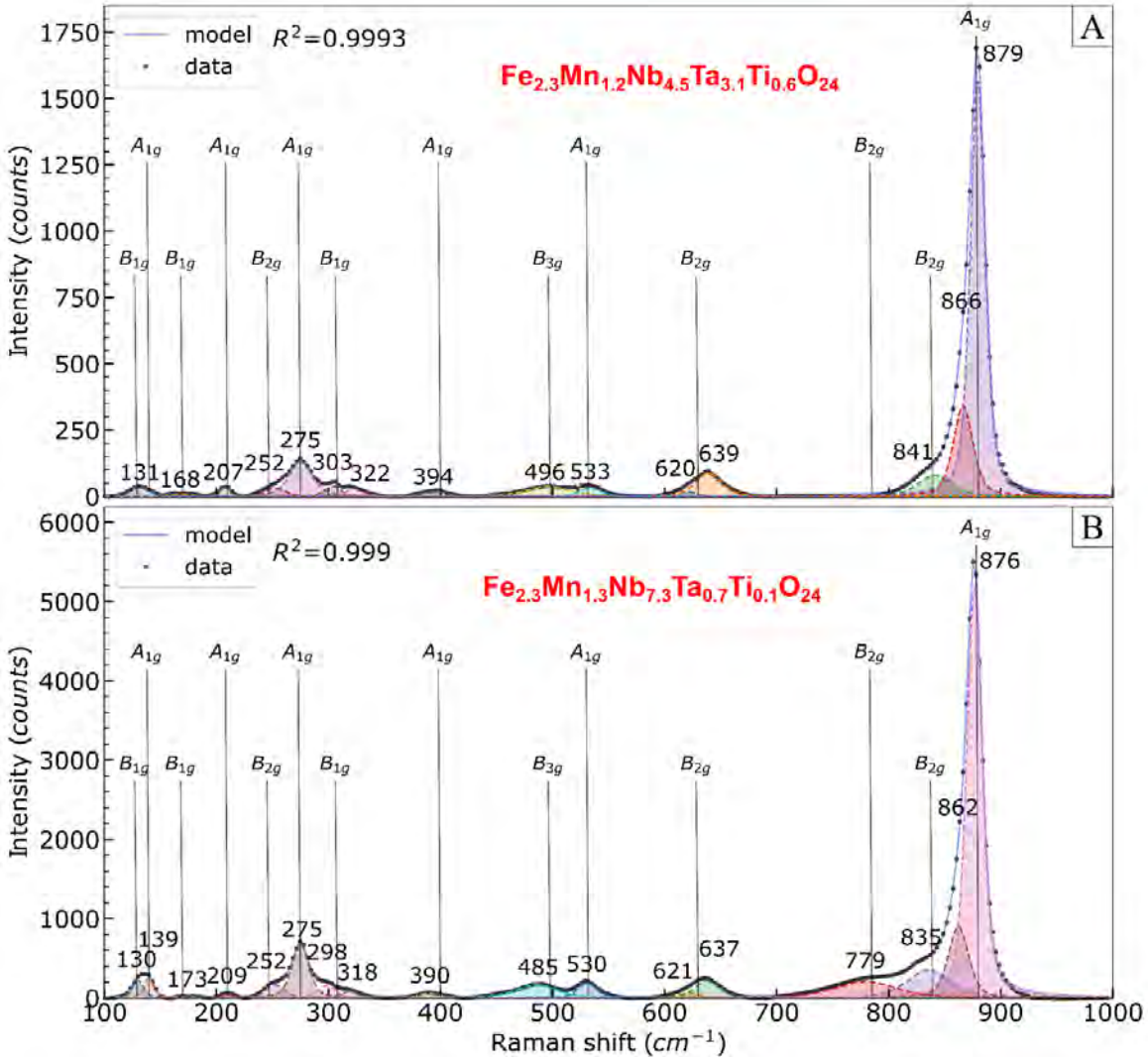

Figure 12: Raman spectra from CGM crystals from the Buranga pegmatite. Analyses from the partially altered phosphatic nodules (BU19TS-ore3-core) in the top image **(a)** and from the albitized facies (BU24-ore1-core) in the bottom image **(b)**. Raman spectra acquired with a 633 nm laser, 150 g/mm grating, 10 % laser power, 100x objective, 30 µm confocal pinhole, two accumulations of 30 s each.

This is the peer-reviewed, final accepted version for American Mineralogist, published by the Mineralogical Society of America.
The published version is subject to change. Cite as Authors (Year) Title. American Mineralogist, in press.
DOI: https://doi.org/10.2138/am-2022-8201. http://www.minsocam.org/

948

Figure 13

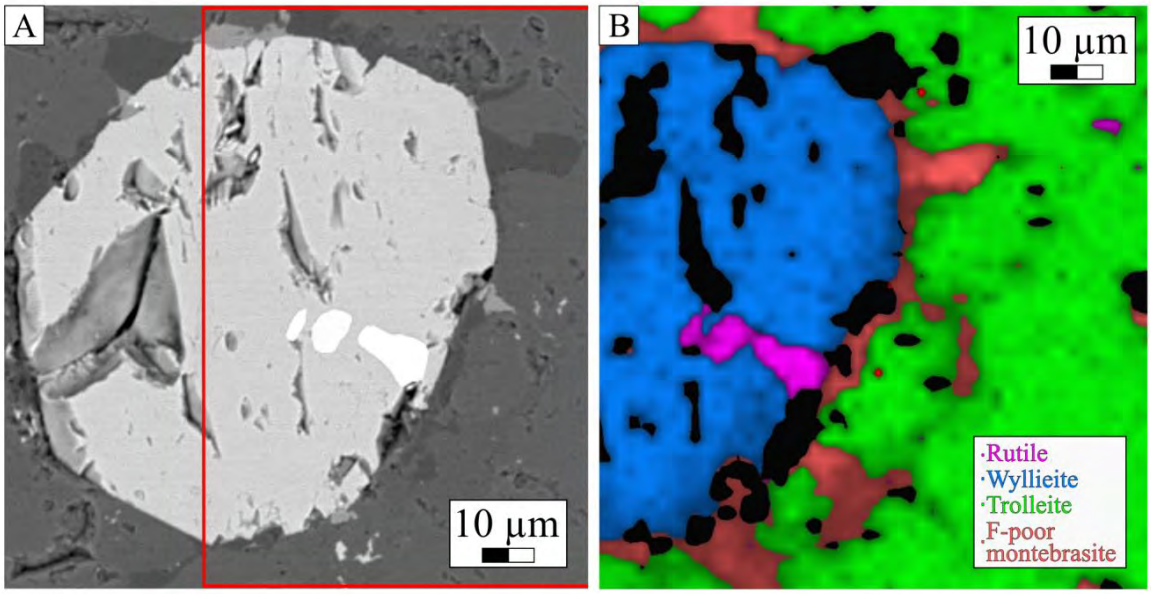

949

950 **Figure 13:** Fe-Nb-Ta-rich rutile included in wyllieite in a partially altered phosphatic nodule. **(a)** BSE image of rutile-wyllieite assemblage.
951 The red box shows the location of (b). **(b)** Classical least squares (CLS) classification map of the assemblage. For details about the classification
952 method and validation, the reader is referred to Araujo et al. (2021). Raman image was acquired in a 2 x 2 µm regular array with a 633 nm laser,
953 150 g/mm grating, 100 % laser power, 100x objective, 100 µm confocal pinhole, single accumulation of 0.3 s, and detector EM gain of 300. The
954 black spots in the image represent holes or areas out of focus.

955

956

957

This is the peer-reviewed, final accepted version for American Mineralogist, published by the Mineralogical Society of America.
The published version is subject to change. Cite as Authors (Year) Title. American Mineralogist, in press.
DOI: https://doi.org/10.2138/am-2022-8201. http://www.minsocam.org/

Figure 14

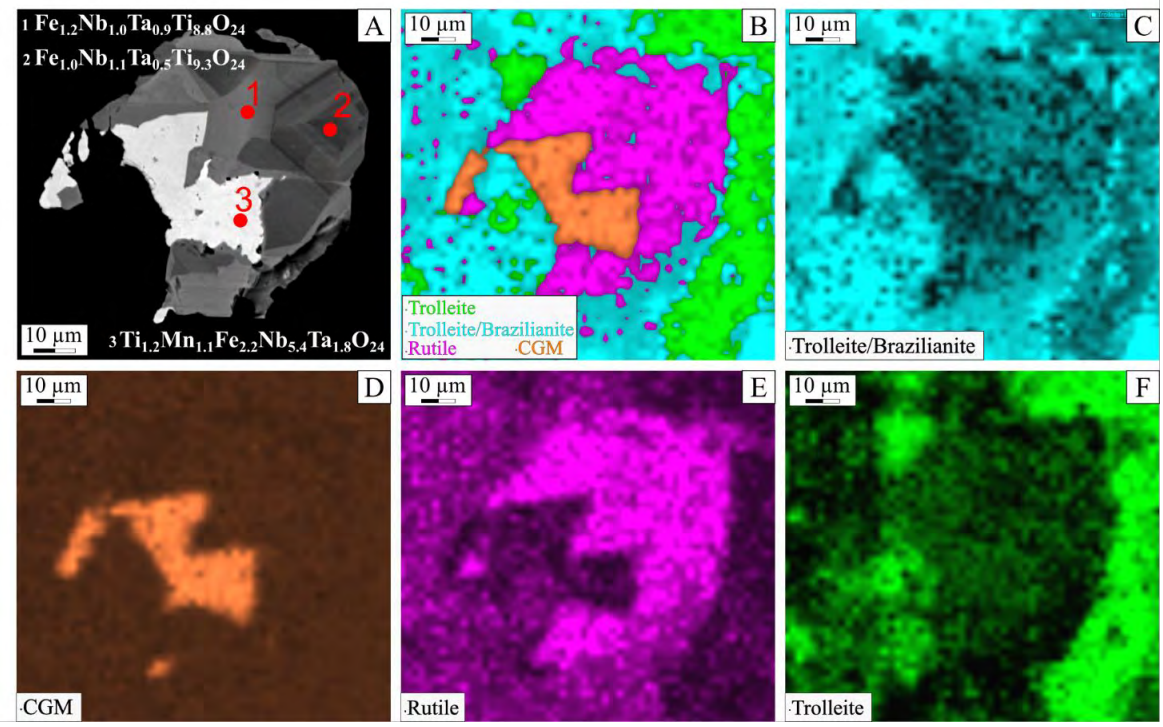

Figure 14: Mixed Fe-Nb-Ta-rich rutile and CGM grain. **(a)** BSE image of the mapped area. The chemical formulae of analyses 1-3 marked on the image are provided. **(b to f)** CLS maps of the assemblage. Raman image was acquired in a 2 x 2 µm regular array with a 532 nm laser, 150 g/mm grating, 25% laser power, 50x long working distance objective, 30 µm confocal pinhole, single accumulation of 0.2 s, and detector EM gain of 500. **(b)** Combined maps showing the spatial distributions of each phase. **(c)** Trolleite/brazilianite phase map. **(d)** CGM phase map. **(e)** Rutile phase map. **(f)** Trolleite phase map.

This is the peer-reviewed, final accepted version for American Mineralogist, published by the Mineralogical Society of America.
The published version is subject to change. Cite as Authors (Year) Title. American Mineralogist, in press.
DOI: https://doi.org/10.2138/am-2022-8201. http://www.minsocam.org/

Figure 15

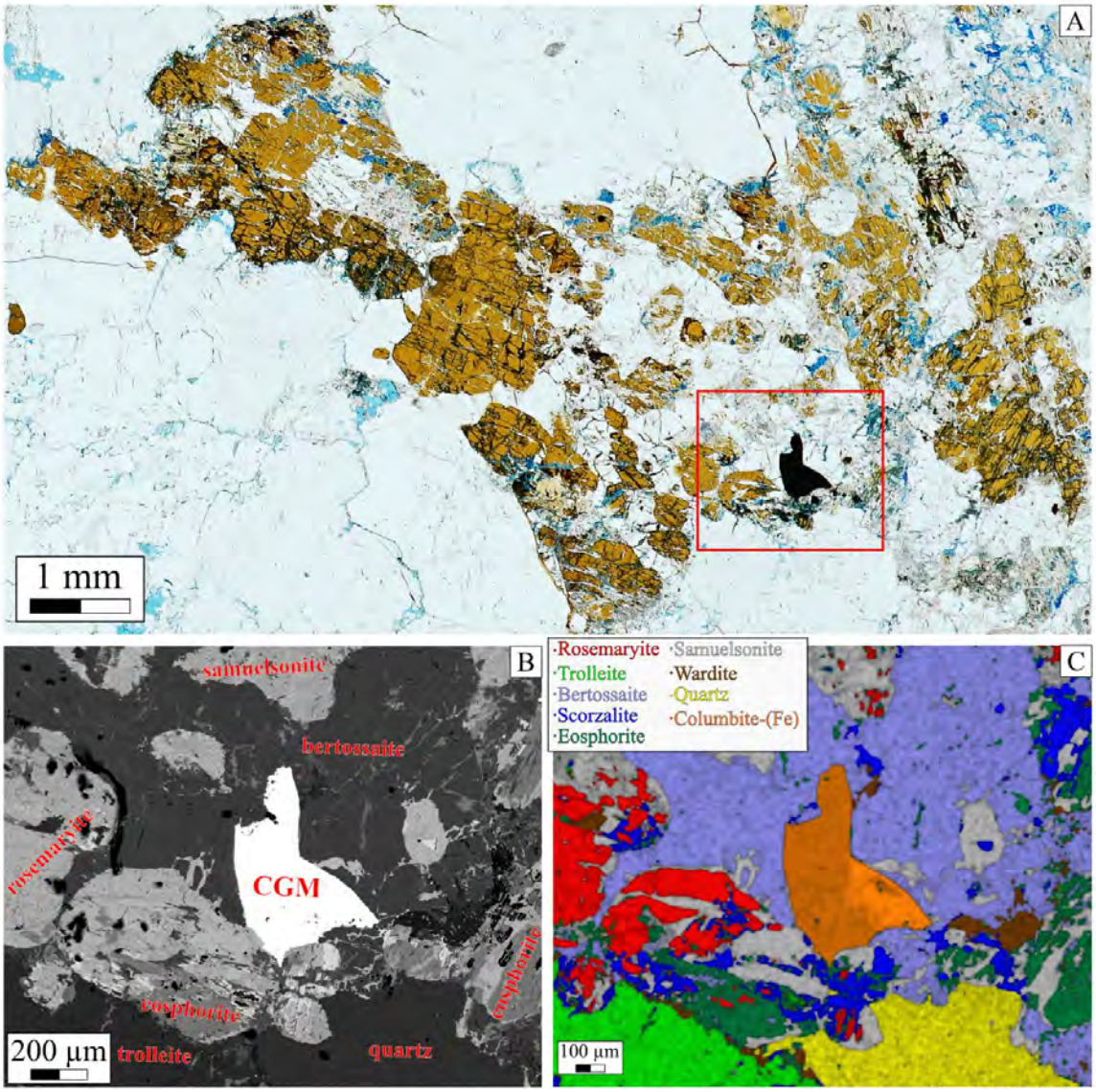

Figure 15: CGM crystal in alteration pod within phosphate minerals. **(a)** Optical photomicrograph of the rosemaryite (brown) pseudomorph partially altered to bertossaite (colorless) hosting CGM (opaque). Parallel polarizers. The red frame marks the location of the Raman map. **(b)** BSE image of the area around the CGM crystal. **(c)** CLS Raman image of the assemblage. The map was acquired in a 5 x 5 µm regular array with a 633 nm laser, 150 g/mm grating, 100% laser power, 50x long working distance objective, 30 µm confocal pinhole, single accumulation of 0.4 s, and detector EM gain of 800.

This is the peer-reviewed, final accepted version for American Mineralogist, published by the Mineralogical Society of America.
The published version is subject to change. Cite as Authors (Year) Title. American Mineralogist, in press.
DOI: https://doi.org/10.2138/am-2022-8201. http://www.minsocam.org/

Figure 16

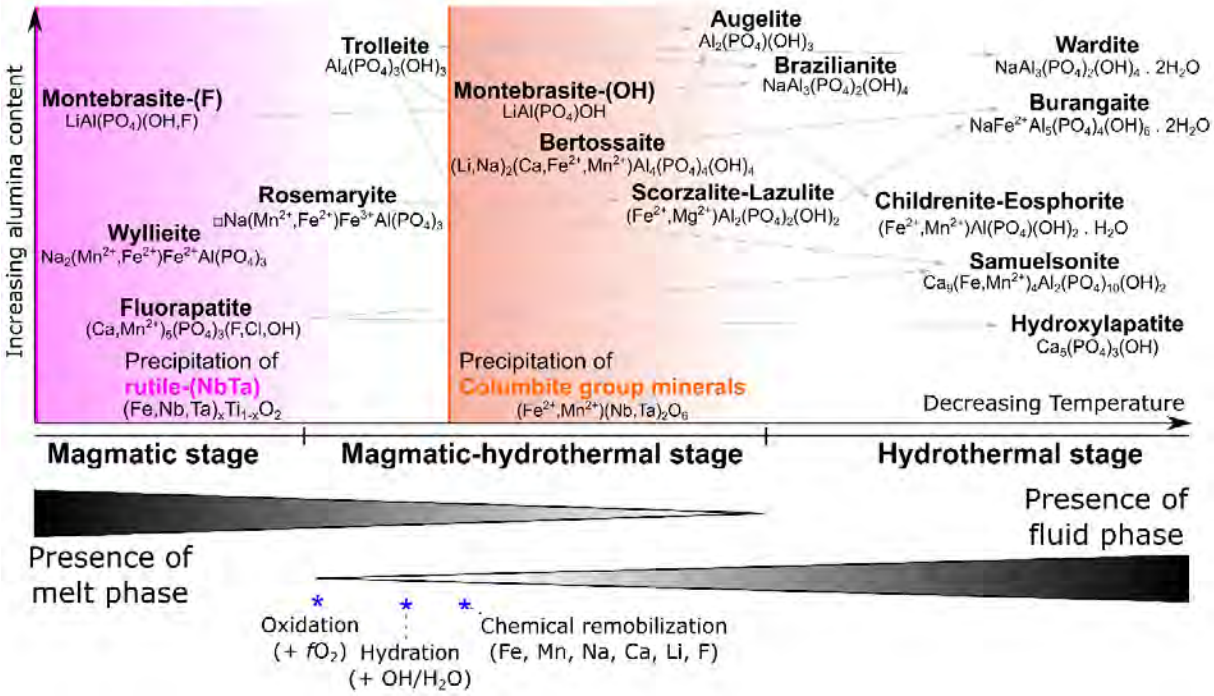

Figure 16: Paragenetic evolution of Nb-Ta oxides and phosphate minerals found in the Al-rich phosphatic nodules of the Buranga according to the alumina content (vertical axis) and crystallization stage (horizontal axis). The precipitation of rutile is marked by the pink field, and of CGM by the orange field. The stages where a melt phase (upper bar) and/or a fluid phase (lower bar) are present are indicated by the gradients from dominant (dark) to subordinate (light). The stages where specific reactions begin to take place (blue asterisks) is also shown. The grey arrows indicate direct formation from a reactive phase to a product phase.

This is the peer-reviewed, final accepted version for American Mineralogist, published by the Mineralogical Society of America.
The published version is subject to change. Cite as Authors (Year) Title. American Mineralogist, in press.
DOI: https://doi.org/10.2138/am-2022-8201. http://www.minsocam.org/

Figure 17

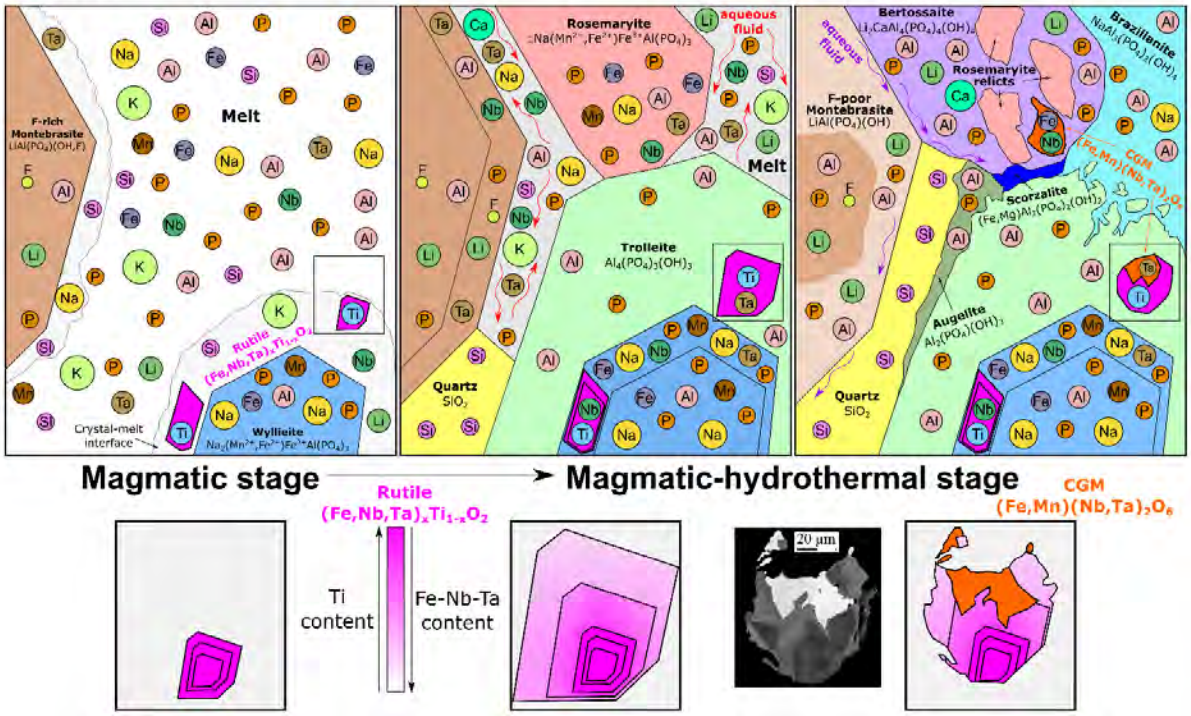

Figure 17: Simplified Nb and Ta mineralization model for phosphorus-rich pegmatites. The initial availability of elements is controlled by the crystallization of phosphate minerals. Firstly, rutile, the only magmatic Nb-Ta-rich mineral, precipitates by disequilibrium crystallization at the crystal-melt interface of magmatic phosphates. Secondly, CGM precipitates when Fe-Mn is released back into the Nb-Ta-bearing residual melt due to dissolution of the primary phases by the exsolved high-temperature aqueous fluid (red arrows) at the magmatic-hydrothermal stage. Elements dissolved in the melt or fixed in a crystal structure are marked by colored circles. Undulated arrows represent the magmatic-hydrothermal fluid circulating in the system. Below is a sketch of the internal evolution of a single NTO crystal during crystallization, this crystal is marked by the square box in the main model.